



Immune regulation enhances osteogenesis and angiogenesis using an injectable thiolated hyaluronic acid hydrogel with lithium-doped nano-hydroxyapatite (Li-nHA) delivery for osteonecrosis

Yue Luo^{a,b}, Zhouyuan Yang^a, Xin Zhao^a, Donghai Li^a, Qianhao Li^a, Yang Wei^c, Luyao Wan^c, Meng Tian^{c,**}, Pengde Kang^{a,*}

^a Department of Orthopedic, West China Hospital, Sichuan University, Chengdu, Sichuan, 610041, PR China

^b Department of Orthopaedics, Affiliated Hospital of North Sichuan Medical College, No. 1 the South of Maoyuan Road, Nanchong, Sichuan, 637000, PR China

^c Department of Neurosurgery and Neurosurgery Research Laboratory, West China Hospital, Sichuan University, Chengdu, Sichuan, 610041, PR China

ARTICLE INFO

Keywords:

Immune regulation
Osteonecrosis
Lithium
Macrophage polarization
Bone regeneration

ABSTRACT

Osteonecrosis is a devastating orthopedic disease in clinic that generally occurs in the femoral head associating with corticosteroid use up to 49 % in patients. In particular, glucocorticoids induced osteonecrosis of the femoral head is closely related to the local immune response that characterized by abnormal macrophage activation and inflammatory cell infiltration at the necrotic site, forming a pro-inflammatory microenvironment dominated by M1 macrophages, and thus leads to failure of bone repair and regeneration. Here, we report a bone regeneration strategy that constructs an immune regulatory biomaterial platform using an injectable thiolated hyaluronic acid hydrogel with lithium-doped nano-hydroxyapatite (Li-nHA@Gel) delivery for osteonecrosis treatment. Li-nHA@Gel achieved a sustain and longterm release of Li ions, which might enhance M2 macrophage polarization through the activation of the JAK1/STAT6/STAT3 signaling pathway, and the following induced pro-repair immune microenvironment mediated the enhancement of the osteogenic and angiogenic differentiation. Moreover, both in vitro and in vivo studies indicated that Li-nHA@Gel enhanced M2 macrophage polarization, osteogenesis, and angiogenesis, and thus promoted the bone and blood vessel formation. Taken together, this novel bone immunomodulatory biomaterial platform that promotes bone regeneration by enhancing M2 macrophage polarization, osteogenesis, and angiogenesis could be a promising strategy for osteonecrosis treatment.

1. Introduction

Osteonecrosis is a devastating orthopedic disease in clinic that generally occurs in the femoral head and is associated with corticosteroid use up to 49 % of patients [1]. The basic pathological changes involve bone cell necrosis, bone trabecular destruction, and inflammatory cell infiltration, which are essentially a sterile inflammatory response induced locally by cell necrosis [2]. In particular, glucocorticoids (GCs) induced osteonecrosis of the femoral head (GI-ONFH) is closely related to the abnormal local immune response mediated by macrophages, wherein the osteonecrosis area was found to be dominated by M1 macrophages and reduced M2/M1 ratio, resulting in a decrease in the secretion of pro-tissue repair factors such as VEGF, BMP2

and TGF- β by M2, which finally inhibited new bone formation and led to difficulties in osteonecrosis repair [3–5], and thus regulation of macrophage phenotypic transformation appears to be a promising approach to treat osteonecrosis such as GI-ONFH. Indeed, immune regulation that creates an osteogenic-friendly microenvironment to effectively promote bone repair and regeneration has attracted considerable interest in recent years for constructing bone related biomaterial platforms [6–12], such as barrier membranes, scaffold, and hydrogels.

Guided bone regeneration membranes (GBRMs) have dominated the market due to their no need for secondary surgical resection, and the adaptation of their outer layer with a Janus structure conferred good bone immunomodulatory effects for bone regeneration [13,14]. Scaffold materials that usually composed of bioceramics or metallic materials

* Corresponding author.

** Corresponding author.

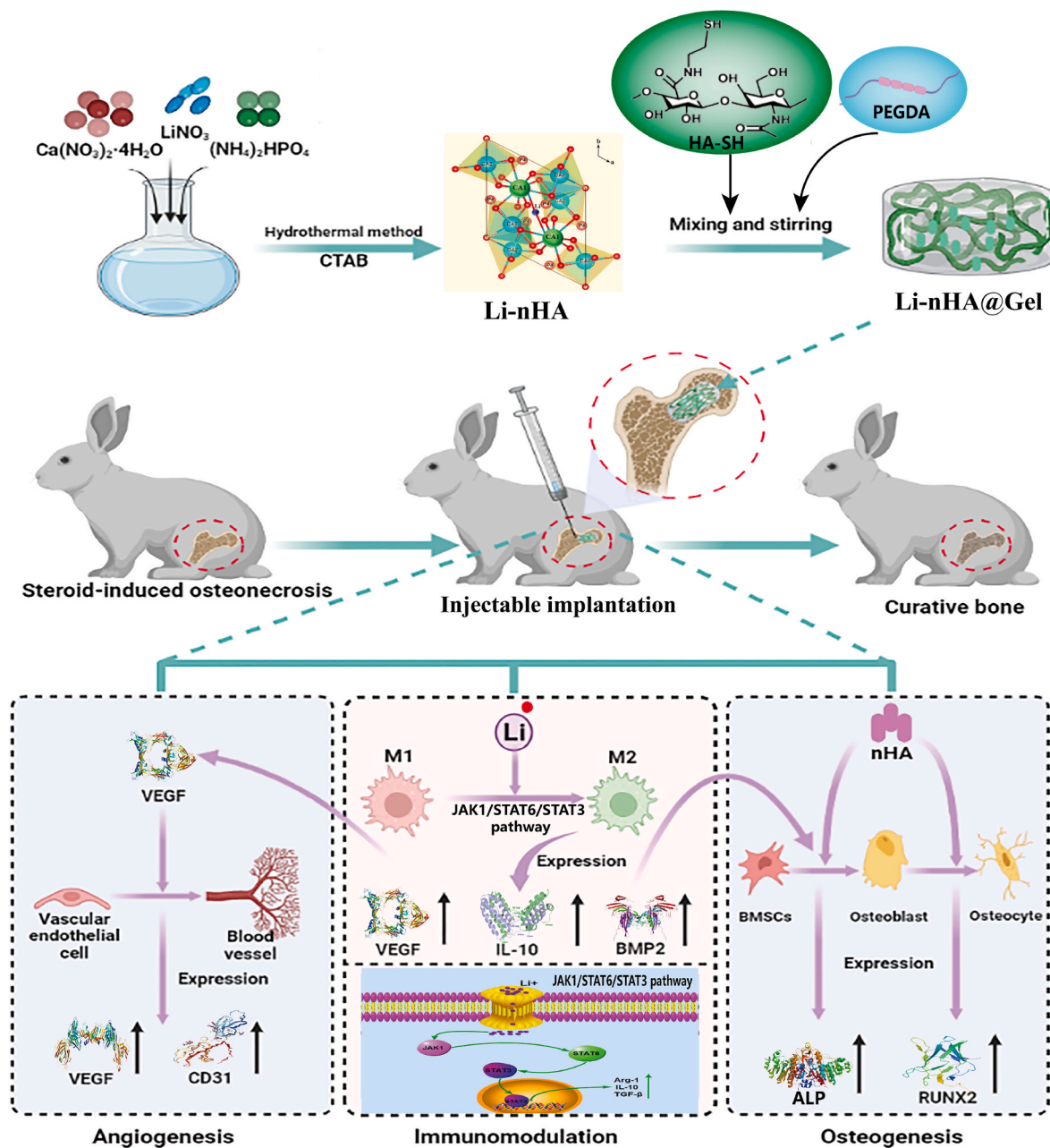
E-mail addresses: tianmeng@scu.edu.cn (M. Tian), kangpengde69@126.com (P. Kang).

<https://doi.org/10.1016/j.mtbio.2024.100976>

Received 20 August 2023; Received in revised form 11 November 2023; Accepted 24 January 2024

Available online 28 January 2024

2590-0064/© 2024 Published by Elsevier Ltd. This is an open access article under the CC BY-NC-ND license (<http://creativecommons.org/licenses/by-nc-nd/4.0/>).



Scheme 1. The summary of fabrication of Li-nHA@Gel and the study on immunomodulation, osteogenesis, and angiogenesis.

have good mechanical properties similar to natural bone and have been widely used in orthopedic implants [15,16]. The scaffold materials can modulate the immune response by changing their microscopic morphology, surface wettability, or carrying bioactive substances, thus build a good immune microenvironment to promote osteogenesis [17–19]. However, both barrier membranes and scaffold materials are poorly plastically, hard to filling irregular defects as well as lack of the advantages of minimally invasive implantation modalities. Alternatively, injectable hydrogels that mimic the natural extracellular matrix (ECM) are capable of being minimally invasive and easy to fill complex defects [20–23]. Moreover, the hydrogels can provide bone immunity through the release of encapsulated cytokines or growth factors such as IL-4 and TGF- β [24,25]. Therefore, injectable hydrogels with plasticity and minimally invasive properties represent a promising platform for osteoimmunomodulatory [26,27].

In terms of immune regulation approaches, both modulation of the materials structure and delivery of biological factors have been

previously mentioned, while metal ions have been recently attracted more and more research interesting as well. Traditionally, metal ions are important trace elements for balancing the body's metabolism and tissue regeneration, which have higher efficacy even at low concentrations due to their chemical stability and low cost [28,29]. Interesting, some metal ions have recently been found to be bioactive in bone regeneration and immune regulation [26–28,30–32]. For example, Huang [30] et al. reported that Cu ions release from micro/nano-topographical coating on a titanium substrate were capable of regulating macrophage polarization as well as macrophage-mediated osteogenic and bactericidal effect, where Cu ions could polarize macrophages to pro-inflammatory M1 phenotype by activating Cu-transport signaling in macrophages. On the contrary, Yang et al. [31] found that Li ions can significantly down-regulate C-C chemokine receptor type 7 (CCR7) and up-regulate the expression of Arg-1, thereby reducing the ratio of M1/M2 and reducing the expression of inflammatory cytokines in macrophages. Likewise, Bartnikowski et al. [32] constructed a lithium

carbonate/polycaprolactone (PCL) scaffold that could induce macrophage conversion to an anti-inflammatory M2 phenotype by down-regulating the expression of inflammatory genes TNF- α , IL-6, and IL-1 β and promoting the expression of IL-10 gene. In general, metal ions are toxic in a dose-dependent manner, and thus it is challenge to achieve a sustainable and controlled release of them to mediate immune cells so as to fulfill their safe and bioactive delivery. However, most of metal ions-containing biomaterials are simply mixing with metal salts using a passive method, which has their innate drawbacks such as sudden release [33]. The burst release causes high concentrations of metal ions around the implant and creates a “high metal ions microenvironment”, which can cause damage to normal cells and reduce cellular activity [34]. To address this issue, the use of carriers for metal ions delivery is necessary to achieve their release in a sustainable and longterm manners. For this regard, thiolated polymers have shown promising due to their metal ions binding ability through sulfhydryl groups along the chains [35].

In clinic, core decompression combined with bone grafting is mainly used to treat the osteonecrosis, where the bone grafting is expected to provide an osteogenic potential for bone formation. Among various bone grafting, bioceramic materials are a class of artificial candidates with good biocompatibility, osteoconductivity, and strong resistance to compression, which can provide not only a favorable local environment for cell proliferation and differentiation, but also can act as an extracellular matrix to guide the reconstruction of defective tissues, making them promising for bone repair and regeneration in clinic [36]. For example, nano-hydroxyapatite (nHA) is the most commonly used bioactive ceramic material as bone grafting [37] due to its chemical and spatial structure similar to that of natural bone tissue [37,38]. Furthermore, nHA is biocompatible and bioactive with osteoconductivity, which can induce bone precursor cells to differentiate and form new bone, and is considered as an excellent bone grafting [39,40]. In addition, osteonecrosis also involves circulatory disruption and endothelial progenitor cell angiogenic dysfunction [41], resulting from that glucocorticoids decrease nitric oxide (NO) activity and induce oxidative stress, which in turn causes apoptosis of vascular endothelial cells and ultimately leads to impaired vascular regeneration [39]. Therefore, angiogenesis is essential in the treatment of osteonecrosis as well [39].

In this work, we report a bone regeneration strategy that constructs an immune regulatory biomaterial platform using an injectable thiolated hyaluronic acid hydrogel with lithium-doped nano-hydroxyapatite (Li-nHA@Gel) delivery for osteonecrosis treatment. We hypothesize that the thiolated hyaluronic acid hydrogel is to delivery the Li-nHA into the osteonecrosis lesion in an injectable operation, but also as a carrier for Li ions release in a sustainable and longterm manners due to doping and binding with sulfhydryl groups that is to enhance M2 macrophage polarization, and thus could modulate the early stage osteoimmune responses, and subsequently mediate the osteogenic and angiogenic differentiation, and finally promote bone regeneration. To address this hypothesis, as shown in Scheme 1, Li-nHA@Gel was first fabricated by loading Li-nHA into an injectable thiolated hyaluronic acid hydrogel, and then in vitro and in vivo studies were carried out to investigate the effects of the Li-nHA@Gel on M2 macrophage polarization, osteogenesis, and angiogenesis. In addition, the possible signaling pathway and mechanism were explored and discussed.

2. Materials and method

2.1. Materials

HA sodium salt from *Streptococcus Equi* was supplied by Aladdin Co., Ltd. (Shanghai, China). 1-(3-Dimethylaminopropyl)-3-ethylcarbodiimide hydrochloride (EDC), N-hydroxysuccinimide (NHS), cysteine, and dithiothreitol (DTT) were obtained from Sigma-Aldrich (St. Louis, MO, USA). Polyethylene glycol diacrylate (PEGDA, MW

3400 Da) was purchased from Thermo Fisher Scientific (Waltham, MA, USA). Alkaline phosphatase (ALP) kit, ARS kit and Triton X-100 were obtained from Beyotime Biotechnology Co. (Jiangsu, China). The Cell Counting Kit-8 (CCK-8) kit was purchased from Thermo Fisher Scientific (Carlsbad, USA), and the live/dead cell staining kit was purchased from Bioss Biotech (Bioss, china). The Other reagents or antibodies, unless specifically mentioned elsewhere, were purchased from Affinity Biosciences, Abcam, Sigma, or GeneTex.

2.2. Li-nHA fabrication and characterization

Lithium doped nano-hydroxyapatite (Li-nHA) was prepared by a hydrothermal method. Briefly, the (Ca + Li)/P molar ratio of HA was kept at 1.67, 100 mL of 0.985 mol/L $\text{Ca}(\text{NO}_3)_2 \cdot 4\text{H}_2\text{O}$ and 0.015 mol/L (use 1.5 % Li-nHA as the optimal concentration, Fig. S1) LiNO_3 solution was added dropwise to 100 mL of 0.6 mol/L $(\text{NH}_4)_2\text{HPO}_4$ solution containing CTAB (molar ratio of $\text{PO}_4^{3-}/\text{CTAB}$ was 1:1). And then a colloidal suspension with white precipitate was obtained and transferred to a Teflon tube. The tube is placed in a sealed stainless steel autoclave and kept at 150 °C for 15 h for annealing. After the sterilizer was cooled to room temperature, the precipitate was separated by filtration and washed sequentially with water and ethanol. Finally, the precipitate was dried in an oven at 80 °C overnight. The dried precipitates were then ground with a mortar and pestle and calcined at 600 °C for 6 h, thereby obtaining Li-nHA nanoparticles. Meanwhile, pure nHA nanoparticles were prepared as a control [42]. The particle diameter of the material was observed by transmission electron microscope (TEM, Hitachi Corporation, Japan). The phase and element composition of the material was analyzed by X-ray diffractometer (XRD, Shimadzu Corporation, Japan). The Fourier Translation Infrared spectroscopy (FTIR) spectrophotometer (Bomem MB-120) was used to analyze the functional groups of the material, and the test wave number range was 400-4000 cm^{-1} , and the resolution was 4 cm^{-1} . Qualitative analysis of elements was performed by X-ray photoelectron spectroscopy (XPS, Philips, the Netherlands).

2.3. Synthesis and characterization of thiolated hyaluronic acid (HA-SH)

In order to activate the carboxyl group of hyaluronic acid, sodium hyaluronate (HA) was dissolved in distilled water, and EDC was added in a certain mole ratio for 15min. Cysteine was added to react for 24 h, and then dialysis was started. Dialysate was changed every day (double steaming water). After dialysis, DTT was added and reacted for 2 h (pH = 8.5), and then dialysis was continued. The dialysis process required nitrogen protection, and the dialysate was replaced every 24 h. HA-SH was obtained by freeze-drying after completion. The chemical structure of the HA-SH was characterized by hydrogen nuclear magnetic resonance spectrometer (^1H NMR, AVANCE III 500 MHz, Bruker). The thiol of the HA-SH was determined by the Ellman method showing a content of 0.48 mmol/g, which corresponded to 24 % of the substitution degree.

The ^1H NMR spectra revealed that the HA-SH showing two new characteristic peaks compared to that of hyaluronic acid, that is, 2.8 and 2.6 ppm peaks corresponding to methylene H and another methylene H near the sulfhydryl group, respectively (Fig. S2).

2.4. Fabrication and characterization of hydrogel composite

PEGDA was dissolved in PBS to obtain a 15 % (w/v) solution. HA-SH was dissolved in PBS. For the preparation of the injectable hydrogel, the PEGDA solution was added to the HA-SH solution with a molar ratio of acrylate/thiol 1:2 to prepare hydrogel precursor solution and initiate crosslinking, where the final concentration of HA-SH was 3 % (w/v). Gelation time was determined by a test tube inverting method. Hydrogel composite was formed by mixing Li-nHA or nHA nanoparticles with hydrogel precursor solution at a volume ratios of 1:2 to ensuring its

injectability.

The internal microstructure of the freeze-dried hydrogel and hydrogel composites was observed using a JEOL-7800F scanning electron microscope (SEM, Japan). The rheological properties of the hydrogel composites were examined using a rotational rheometer (Anton Paar MCR302, Austria). The storage modulus (G') and loss modulus (G'') of the samples were measured in the frequency range of 0.1–10 Hz with an 8 mm diameter probe in sweep mode. The elastic modulus of hydrogel composites was determined as the average storage modulus at 1 Hz for each sample ($n = 3$). To determine the compression modulus of each sample ($\Phi 10 \text{ mm} \times 6 \text{ mm}$), a universal testing machine (AG-Instron) was used to apply a uniaxial compression force (displacement rate of 2 mm/min and load of 0.05 N). The compression modulus was obtained from a linear fit of the stress-strain curve.

The hydrogel or hydrogel composite was respectively placed in PBS and incubated at 37 °C for 48 h to analyze their swelling ratio. The formula was calculated as follows: $(W1 - W0)/W0 \times 100 \%$, where $W1$ was the weight of hydrogel or hydrogel composite at 48 h, and $W0$ was the initial weight of hydrogel or hydrogel composite ($n = 3$). In vitro degradation was detected by weight loss of hydrogel composites in PBS solution (0.01 M, pH 7.4) at 37 °C. The hydrogel composites were removed and weighed as Wt at the set time point. The in vitro degradation rate was calculated as: $\text{weight remaining (\%)} = Wt/W0 \times 100 \%$, where $W0$ is the initial weight of the hydrogel composites and Wt is the weight of hydrogel composites at the set time point. The cumulative release of Li^+ was analyzed by inductively coupled plasma mass spectrometry (ICP-OES, Agilent, USA). The hydrogel composite was immersed in lithium-free simulated body fluid (SBF, pH = 7.4) and maintained at 37 °C for 28 days (set day 1, 3, 7, 14, 21, and 28 as each determination time point).

2.5. In vitro cell compatibility assay

Rabbit BMSCs were isolated and cultured for identification (Figs. S3 and S4). To assess the effect of hydrogel composites on the cell viability of BMSCs, BMSCs cells (4×10^4 /well, 24-well plates) were co-cultured with hydrogel composites for 4 days with the aid of Transwell cell culture chambers (Corning Life Sciences, Corning, NY, USA) before using a live/dead cell staining kit consisting of Calcein-AM (green fluorescence) and Propidium Iodide (PI, red fluorescence) (Bioss, china) to assess cell viability and fluorescence was observed with a laser scanning confocal microscope (Olympus, Japan).

The hydrogel composites were incubated with BMSCs (5×10^3 /well) for 3 and 7 days, and the cytotoxicity and proliferation capacity of the hydrogel composites were evaluated using Cell Counting Kit-8 (CCK-8, Thermo Fisher Scientific, Carlsbad, USA).

2.6. The effect of hydrogel composites on macrophage polarization and inflammatory response

To mimic the GCs induced osteonecrosis environment in vitro, dexamethasone treatment was used in this study [43]. Utilizing 0.4 μm membrane pore size 12-Transwell cell culture chambers (Corning Life Sciences, Corning, NY, USA), 10^{-6} mol/L dexamethasone preconditioned macrophages (RAW264.7, 1×10^5 /well) were inoculated in the lower chamber of the 12-well plate co-culture system for 24h, followed by 100 μl of hydrogel composites or hydrogel was placed in the upper chamber Incubation. The culture medium was changed every 24 h.

After 4 days of culture, the M1 and M2 macrophages were identified by flow cytometry and immunofluorescence staining, and related genes expression (IL4, IL6, IL10, TNF- α , BMP-2, and VEGF) was determined by qPCR. To investigate the activation of JAK1/STAT6/STAT3 signaling pathway, Western blot analysis and qPCR were used to analyze the related proteins and genes of phosphorylated JAK1 (p-JAK1), phosphorylated STAT3 (p-STAT3), and phosphorylated STAT6 (p-STAT6). The primary antibodies: RUNX2 (1:500, abcam), ALP (1:500, abcam), P-

JAK1 and P-JAK1, P-STAT3 and P-STAT3, P-STAT6 and P-STAT6 (1:1000, abcam), and β -Actin (1:2000, abcam).

For immunofluorescence staining, the samples were fixed with 4 % paraformaldehyde for 15 min, and then permeated with 0.5 % Triton X-100 at room temperature for 10 min. Then 5 % donkey serum was used for 30min. After that, the 1:100 diluted CCR7 (abcam) and Arg-1 (abcam) primary antibodies were added to the sample and incubated overnight at 4 °C. Then the coverslips were incubated with the respective fluorescein isothiocyanate-conjugated or tetramethylrhodamine isothiocyanate-conjugated secondary antibody for 45 min, followed by 10 min of nuclear staining with DAPI. The samples were observed with a fully automatic inverted fluorescence microscope (Olympus X83, Japan).

Total RNA was isolated using Cell Total RNA Isolation Kit (Foregene, chengdu, China) adapted from the manufacturer's protocol and reverse-transcribed with RT Easy TM I Master Premix (Foregene, chengdu, China) to synthesize the cDNA. The expression level of the target genes was evaluated with the primers listed in Table S1, with reference to the GAPDH as the housekeeping gene. Finally, quantitative gene analysis was performed by RT-PCR (Bio-rad, UK).

2.7. Behavior of BMSCs or HUVECs with in conditioned medium (CM) of macrophages pretreated with hydrogel composites

RAW 264.7 (1×10^5 /well) were co-cultured with 100 μl of hydrogel composite or hydrogel for 4 days using the Transwell co-culture system. The culture supernatant was collected and diluted at a ratio of 1:2 with DMEM containing 10 % fetal bovine serum before use. The prepared conditioned medium was denoted as Gel-CM, nHA@Gel-CM, and Li-nHA@Gel-CM based on the corresponding hydrogel composites with which the macrophages were cultured. The osteogenic differentiation of BMSC was measured using alkaline phosphatase (ALP) staining and a calcium deposition assay. BMSCs were cultured in Gel-CM, nHA@Gel-CM, and Li-nHA@Gel-CM medium for 21 days, changing the medium every 72 h. The cells were then washed and stained with an alkaline phosphatase (ALP) staining reagent (Beyotime, China) and Alizarin Red S (ARS) staining (Cyagen, USA). The expression levels of osteogenic associated proteins ALP and Runx2 were detected by Western-blot.

The migration and angiogenesis of HUVECs cells were measured by cell scratch and tube formation assay. In the cell scratch experiment, HUVECs were briefly inoculated on 24-well plates with 5×10^4 cells per well. After 24h of culture, 1 mL pipetting spear head was used to make a scratch along the central axis, and then cleaned with PBS. Meanwhile, the scratch site was photographed using an inverted fluorescence microscope (Zeiss, Germany). Gel-CM, nHA@Gel-CM, and Li-nHA@Gel-CM medium were added, and photos were taken at the same location after 12 and 24h of culture. In the tube formation assay, the Matrigel matrix was briefly thawed overnight in a refrigerator at 4 °C. On the next day, 100 μl Matrigel matrix gel/well was laid on the 24-well plate on ice, and then gelled in the incubator at 37 °C for 30min. After adjusting the cell concentration, HUVECs were inoculated on the matrix gel at 1×10^5 cells/well. 300 μl of the conditioned media (Gel-CM, nHA@Gel-CM, and Li-nHA@Gel-CM) and the positive control group (50 $\mu\text{g}/\text{mL}$ VEGF recombinant protein) were added to each well, and cultured at 37 °C in 5 % CO_2 for 6–24h. The microvascular formation was observed under an inverted fluorescence microscope. Image j V1.8.0 Image processing software (NIH, USA) was used to calculate the number of vascular branches and the total length of vascular branches, and the rate of wound healing was measured to determine the migration ability of cells. The expression levels of angiogenic factors CD31 and MMP9 were detected by RT-PCR (Table S1).

2.8. In vivo study

All animal experiments processed under the protocol approved by the Animal Ethical Committee of West China Hospital of Sichuan

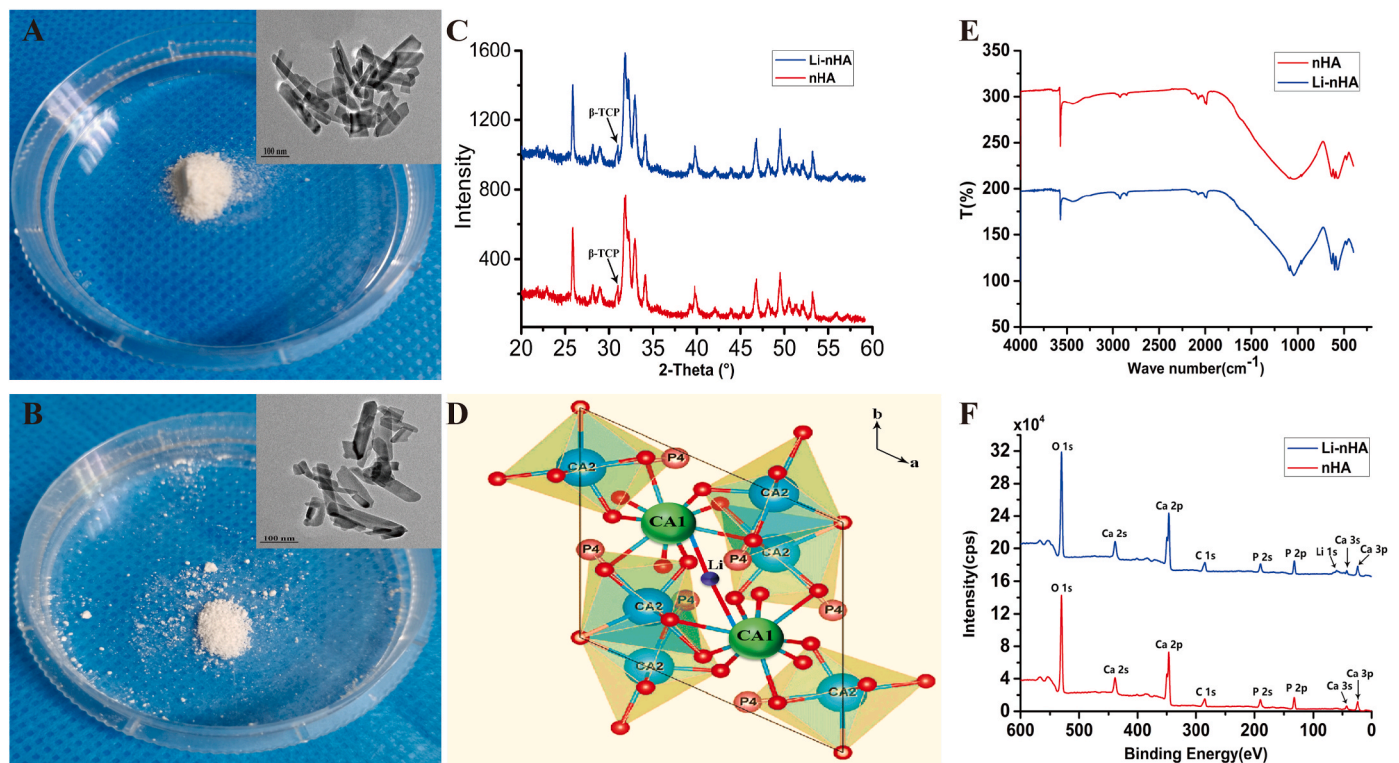


Fig. 1. The physical property characterization of Li-nHA. (A) General view of Li-nHA powder and TEM image of Li-nHA. The scale is 100 nm. (B) General view of nHA powder and TEM image of nHA. The scale is 100 nm. (C) The phase composition of Li-nHA and nHA was analyzed by X-ray diffraction (XRD). (D) The three-dimensional crystal structure and the schematic planar structure of Li-nHA nanoparticles. (E–F) Fourier transform infrared spectroscopy (FTIR) (E) and X-ray photoelectron spectroscopy (XPS) (F) of the Li-nHA and nHA.

University (2019111A). A total of 44 New Zealand White rabbits were selected to establish a GI-ONFH model, 4 were used to verify the effect of drilling and material implantation, and the remaining 40 were used for hydrogel composites implantation in each group. The 40 rabbits were randomly assigned to four groups: Blank control (10 rabbits, 20 femoral head); Gel scaffold (10 rabbits, 20 femoral head); nHA@Gel scaffold (10 rabbits, 20 femoral head); Li-nHA@Gel scaffold (10 rabbits, 20 femoral head). As previously mentioned, a defect channel 3 mm in diameter and 5 mm in length was drilled from the femoral neck to the femoral head. These materials were then implanted into the femoral head defect. Rabbits in each group were euthanized at 1, 4 and 12 weeks after surgery ($n = 8$ for 1 week, $n = 32$ for 4 and 12 week). The changes of M1 (CCR7) and M2 (Arg-1) macrophages were detected in rabbits sacrificed at 1 weeks. Histological analysis and imaging analysis were performed on rabbits sacrificed at 4 and 12 weeks to examine the osteogenic effect of the scaffolds. A micro-CT system (Inveon MultiModality Gantry-STD CT) was used for evaluating the bone regeneration in the bone defect following ONFH as pre-described [44]. The bone volume fraction (bone volume/total volume and bone mineral density) was analyzed as previously described [44].

2.9. Histological and histometric analysis

The femoral head samples were fixed in 10 % formaldehyde for a week, and then decalcified in 20 % EDTA solution for about 3 months and dehydrated through a gradient ethanol series, cleared in xylene and embedded in paraffin. Sections of 4 mm thickness were made and stored at a temperature of 37 °C. The sections were stained with haematoxylin and eosin (HE), and Masson's trichrome. Finally, each piece of the sections was observed using a light microscope (BX41, Olympus, Japan). HE staining images were used to calculate the percentage of the new bone area in the defect regions via histomorphometry, and the data were analyzed using the Image Pro-Plus 7.0 software. The following equation

was used: New bone formation area (%) = New bone formation area/ bone defect area \times 100 %. The vascular-like structures formed in the HE or Masson images were assayed under a light microscope (BX41, Olympus, Japan). The number of vascular-like rings was then calculated.

2.10. Immunofluorescence histochemical analysis

To assess in vivo macrophage phenotypic changes, osteogenesis and angiogenesis, the expression of Arg-1, CCR7, Runx2 and CD31 in the implants was measured by immunofluorescence histochemistry. The specimens were fixed in 4 % paraformaldehyde for 20 min and then dehydrated successively with gradient concentrations of ethanol. The dehydrated specimens were embedded in paraffin and frozen sectioned. Section samples were rehydrated in continuous dilution of ethanol and incubated in a PBS buffer consisting of 10 % goat serum, 5 % BSA and 0.5 % Triton X-100. Runx2 (Affinity Biosciences), CD31 (GeneTex), Arg-1 (abcam) and CCR7 (abcam) in 1:100 dilution were used for immunofluorescence staining. Alexa-fluor labeled goat anti-mouse IgG or Alexa-Fluor labeled goat anti-rabbit IgG (Invitrogen) were then incubated as secondary antibodies, and finally stained with DAPI. The integral optical density (IOD) was calculated with Image Pro Plus 7.0 software.

2.11. Statistical analysis

All analyses were performed using GraphPad Prism 6 (GraphPad Software, USA). Quantitative data were expressed as mean \pm SD, and differences between groups were evaluated using one-way ANOVA and Tukey's multiple comparison test, with $p < 0.05$, $P < 0.01$, and $P < 0.001$ indicating the statistical significance.

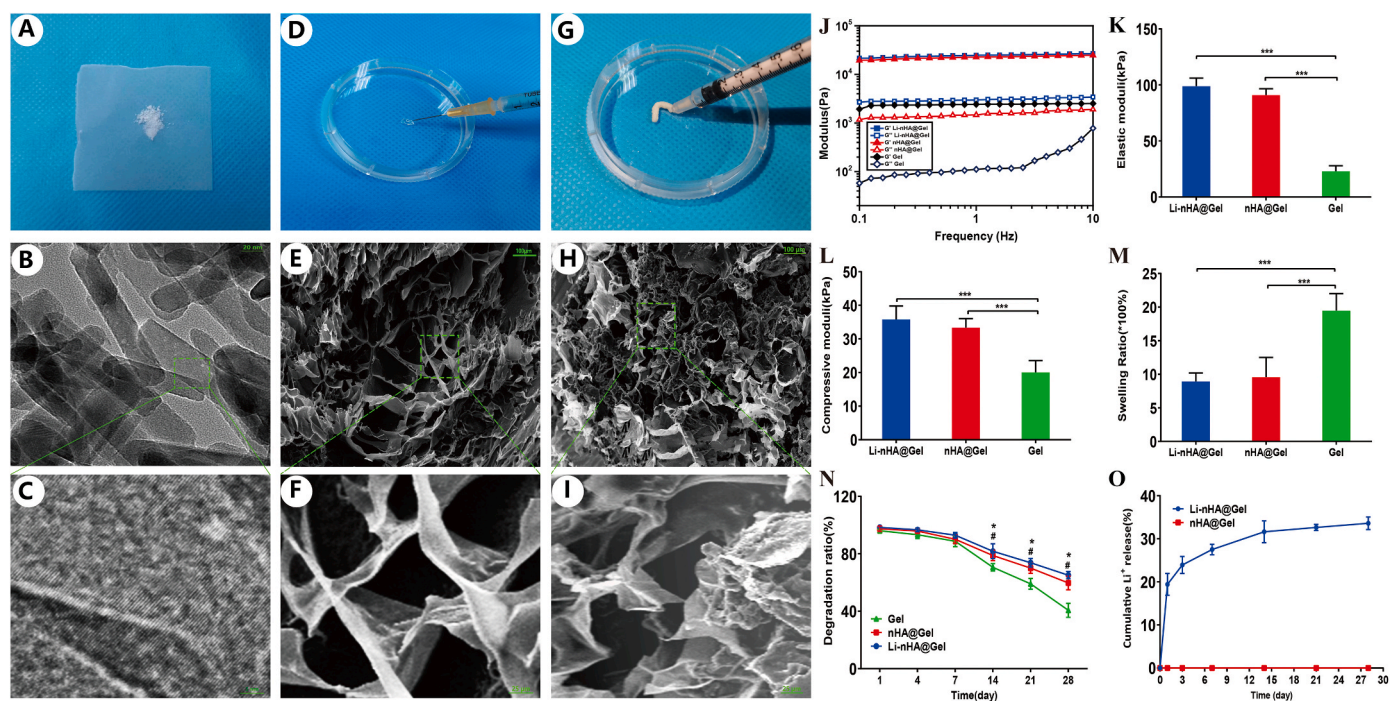


Fig. 2. The physical property characterization of hydrogel composite scaffold materials. (A–C) General view of Li-nHA powder (A) and TEM image of Li-nHA (B and C). The scale is 100 nm. (D–F) Macroscopic processes of hydrogel (Gel) injectability (D) and SEM images of hydrogels (E and F). (G–I) Macroscopic processes of Li-nHA@Gel injectability (G) and SEM images of Li-nHA@Gel (H and I). (J) Rheological measurements of hydrogels. (K) The average modulus of elasticity of the scaffold material at 1 Hz. (L) The average compressive modulus of the scaffold material. (M) Equilibrium swelling studies of scaffold materials under PBS incubation at 37 °C. (N) Degradation tests of the scaffold materials. * $P < 0.05$ refers to a statistically significant difference between Li-nHA@Gel and Gel, and # $P < 0.05$ refers to a statistically significant difference between nHA@Gel and Gel. (O) Cumulative release curves of Li ions from Li-nHA@Gel and nHA@Gel in SBF. (* $P < 0.05$, ** $P < 0.01$, and *** $P < 0.001$ represent statistically significant differences between groups).

3. Results and discussion

3.1. Fabrication and characterization of Li-nHA

Both Li-nHA and nHA nanoparticles were prepared by a hydrothermal method using cetyltrimethylammonium bromide (CTAB) as a template (Fig. S5). The appearance of the obtained products is shown in Fig. 1A and B, both of which are similar giving white powders. TEM was used to observe the morphology of the nanoparticles. As shown in Fig. 1A and B insets, both Li-nHA and nHA nanoparticles are rod-shaped with diameter 20–45 nm and length 50–150 nm. The chemical structure of the Li-nHA and nHA were characterized by XRD, FTIR, and XPS. The XRD pattern shows that Li-nHA has essentially the same diffraction peaks as nHA without new peaks, both of which accompanied by weak diffraction peaks of β -tricalcium phosphate (Fig. 1C). Moreover, due to the small ionic radius of lithium and low dose doping, the XRD spectrum of Li-nHA has the same hexagonal diffraction plane as that of standard nHA (JCPDS # 09–0432), indicating that the low dose of Li doping into nHA did not change the crystal structure of nHA [42,45]. In general, whether the Li doping into nHA is by way of Li ions replacing Ca ion positions or as an additional atom inserted into the nHA structure (interstitial atoms) depends mainly on the peak intensity, peak width, and the presence of lithium phosphate peaks in the XRD pattern [46]. And these are the only two ways of lithium doping into nHA reported in the literature so far. Therefore, if the peak intensity decreases, the peak width increases, or the presence of lithium phosphate peaks in the XRD pattern, it indicates that lithium doping in nHA is achieved by replacing the Ca ion position with lithium ions [47]. However, the XRD spectra of Li-nHA in this study did not show the above mentioned situations, so it was concluded that the lithium doping in nHA in this study was achieved by inserting an additional lithium atom into the nHA structure (Fig. 1D), and it was also confirmed that lithium was successfully doped into nHA.

The FTIR spectra show similar characteristic peaks for Li-nHA and nHA, which indicates that low levels of doped lithium have no effect on the FTIR spectra of nHA (Fig. 1E). XPS results show that a typical small Li diffraction peak is appeared in the spectrum of the Li-nHA, which indicate that lithium is successfully doped into nHA (Fig. 1F).

3.2. Fabrication and characterization of Li-nHA@Gel

The injectable hyaluronic acid hydrogel was prepared by Michael addition reaction between the thiols in the HA-SH and acrylates in the PEGDA to form a three-dimensional network under physiological conditions. The molar ratio of thiols to acrylates was set at 2/1 to ensure that the remaining sulfhydryl groups for Li ions binding in the hydrogel. The gelation time of the hydrogel was 8.6 ± 1.6 min, which was in the range of the clinical operation time (5–15 min). The hydrogel composite was fabricated by mixing Li-nHA powder (Fig. 2A–C) with hydrogel precursor solution (Fig. 2D–F), and the injectable operation is shown in Fig. 2G within the gelation time. The surface morphology of the Li-nHA powder was shown in Fig. 2B and C using TEM. The internal microstructure of the freeze-dried hydrogel and hydrogel composite was observed using SEM (Fig. 2E–F and 2H–I, Fig. S6), and each composite had a three-dimensionally interconnected porous structure with a pore size range of 100–300 μm , which would be beneficial for cell infiltration and the exchange of nutrients and metabolites [48].

The storage (G') and loss modulus (G'') were measured with a plate-rheometer. The maximum G' for the Li-nHA@Gel and nHA@Gel was significantly higher than that of hydrogel alone, indicating that the presence of the nanoparticles in the hydrogel increased the mechanical strength (Fig. 2J). Consistently, the elastic modulus of the Li-nHA@Gel and nHA@Gel were 99 ± 7.1 and 91.1 ± 5.5 kPa, respectively, which were significantly higher than that of the hydrogel alone (23.0 ± 4.9 kPa) ($P < 0.05$, Fig. 2K). Also, with the incorporation of Li-nHA or nHA

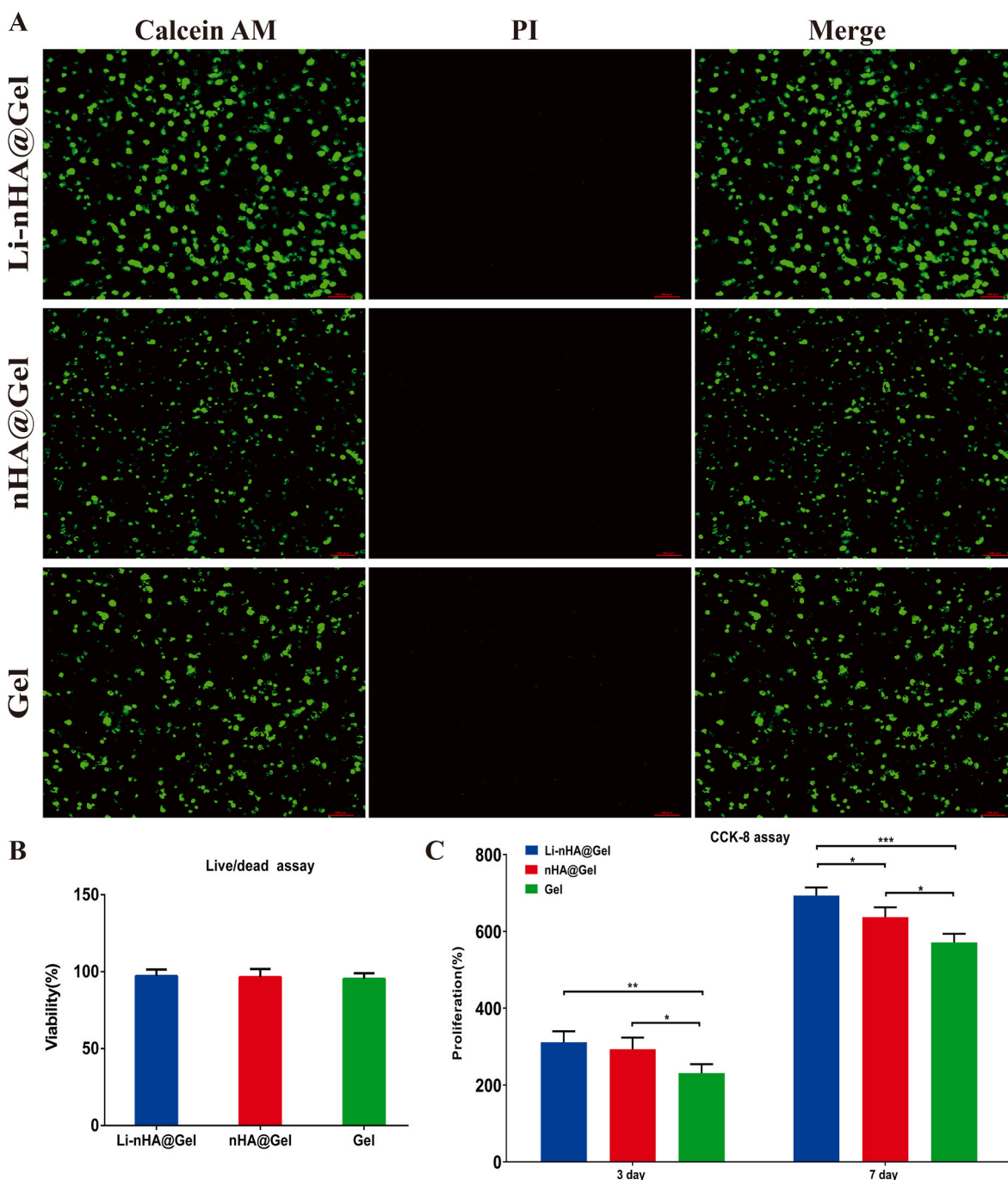


Fig. 3. The cytocompatibility assay of the hydrogel composites. (A) Live/Dead assay of BMSCs on hydrogel composites after cultured for 4 days, green indicates live cells and red indicates dead cells, the scale bar indicates 100 μm . (B) Percentage of viable BMSCs on hydrogel composites after 4 days of culture. (C) The CCK-8 method was used to evaluate the cell proliferation ability of scaffold materials after co-culture with BMSCs for 3 and 7 days. (* $P < 0.05$, ** $P < 0.01$, and *** $P < 0.001$ represent statistically significant differences between groups). (For interpretation of the references to color in this figure legend, the reader is referred to the Web version of this article.)

into the hydrogel, a significant increase of the compressive modulus was observed (Fig. 2L). The above results suggest that the incorporation of the nanoparticles improved the mechanical properties of the hydrogel composites [49], which will provide better mechanical support for osteonecrosis treatment compared to hydrogel alone. Moreover, in the osteogenic microenvironment, the increase of the mechanical strength of the grafting materials is expected to be beneficial to promote the osteogenic differentiation of the stem cells [50].

The swelling property of the hydrogels is indispensable for substance exchange, and their equilibrium swelling ratio directly reflects the

efficiency of substance metabolism [51]. After incubation in physiological conditions (PBS at 37 $^{\circ}\text{C}$) for 48 h, the swelling ratio of Li-nHA@Gel and nHA@Gel were $893.5 \pm 126\%$ and $957.2 \pm 292.1\%$, respectively, which were significantly lower than that of Gel ($1949 \pm 251.4\%$, Fig. 2M). The reasons for the results may be that the dense microstructure possessed by Li-nHA@Gel and nHA@Gel reduces the water retention space compared to hydrogels alone [52]. In addition, the swelling ratios of Li-nHA@Gel and nHA@Gel were similar, indicating that Li-nHA@Gel and nHA@Gel reduced the water absorption capacity of the hydrogels to a similar extent.

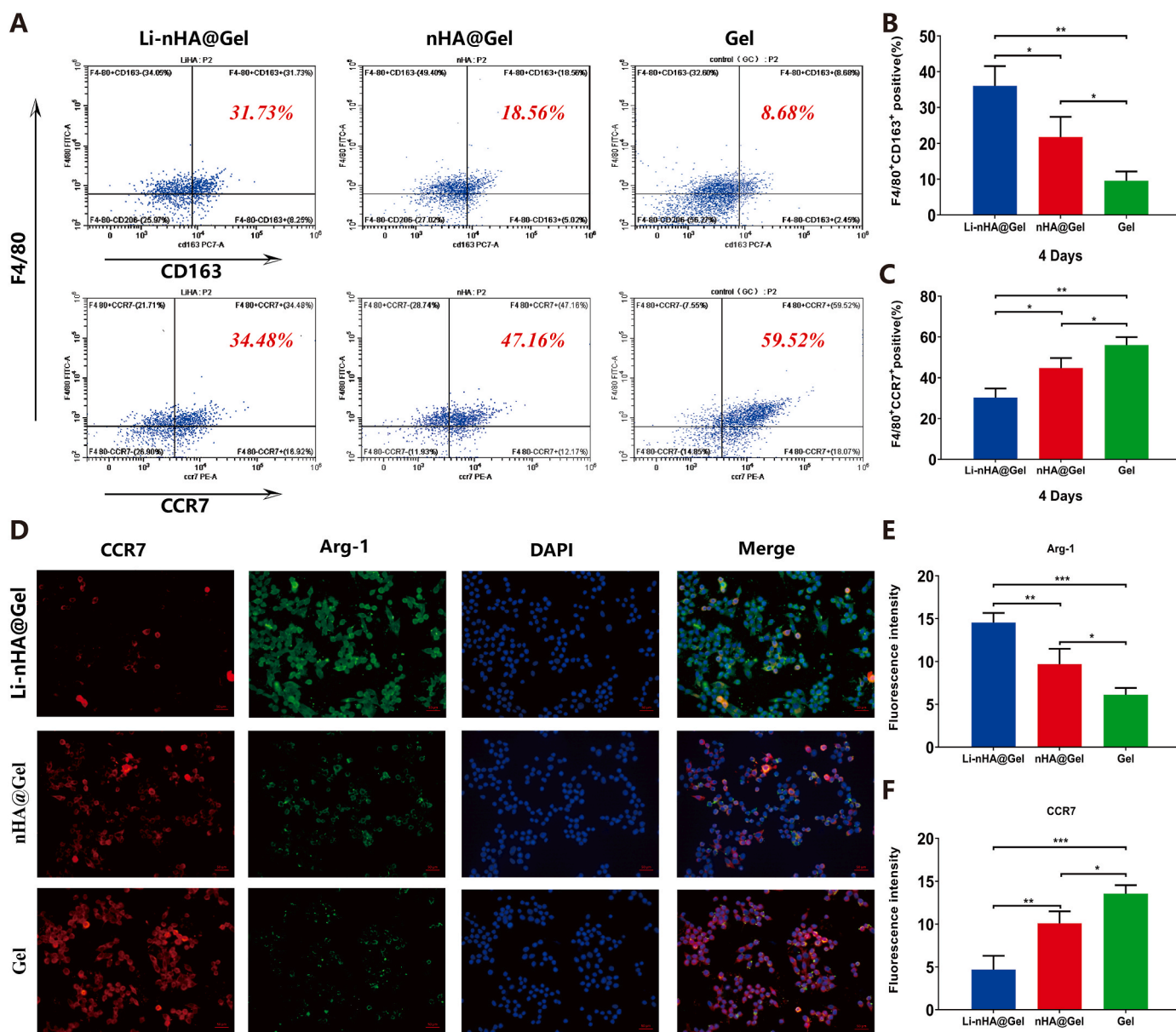


Fig. 4. Li-nHA@Gel regulates macrophage polarization. (A) Flow cytometry patterns of macrophages F4/80 (M), CD163 (M2) and CCR7 (M1) antibodies in RAW264.7 cells treated with glucocorticoid by Li-nHA@Gel and nHA@Gel after 4 days. (B–C) The percentage of F4/80 and CCR7 (M1) and F4/80 and CD163 (M2) double positive cells. (D) An immunofluorescent image of a glucocorticoid-pretreated Raw264.7 macrophage treated by Li-nHA@Gel and nHA@Gel shows Arg1 (green) and CCR7 (red) antibody staining and the nucleus (blue). The scale is 50 μ m. (E–F) Quantitative analysis by immunofluorescence staining. (* $P < 0.05$, ** $P < 0.01$, and *** $P < 0.001$ represent statistically significant differences between groups). (For interpretation of the references to color in this figure legend, the reader is referred to the Web version of this article.)

The in vitro degradation behaviors of the hydrogel composites are shown in Fig. 2N. The weight of all samples decreased with the time prolonged, especially the degradation of the hydrogel alone was particularly pronounced, while the degradation of the Li-nHA@Gel and nHA@Gel were significantly lower after 14 days. The above results confirm that the hydrogel composites have good physicochemical stability and are expected to support the long-term growth and proliferation of osteogenic stem cells in vivo [53]. For the release assay, the release rate of Li^+ from Li-nHA@Gel was linear on the 1st day, gradually slowed down from the 3rd to the 7th day, and reached a plateau on the 14th day, with about $33.6 \pm 1.5\%$ of Li^+ released in SBF on the 28th day (Fig. 2O), which demonstrated the hydrogel composite was capable of sustained and longterm release of Li^+ . In addition, Li^+ was not significantly detected in nHA@Gel.

3.3. Cell compatibility

The live/dead staining results showed a high viability (>90 %) for all groups after 4 days of co-culture (Fig. 3A and B), which verified the good cell compatibility of all samples. The results of CCK-8 assay revealed that all groups were able to sustain the growth and proliferation of BMSCs. Moreover, both Li-nHA@Gel and nHA@Gel groups promoted the proliferation of BMSCs compared to the Gel group ($P < 0.05$). This may be due to the similar chemical structure of nHA and bioapatite that can provide a suitable environment for cell adhesion and proliferation [54]. Interestingly, the cell proliferation in the Li-nHA@Gel group was higher than that in the nHA@Gel group on day 7 ($P < 0.05$), which may be related to the release of lithium ions from the hydrogel composite (Fig. 3C). All these results indicate that the hydrogel with or without Li-nHA/nHA is cytocompatible in vitro.

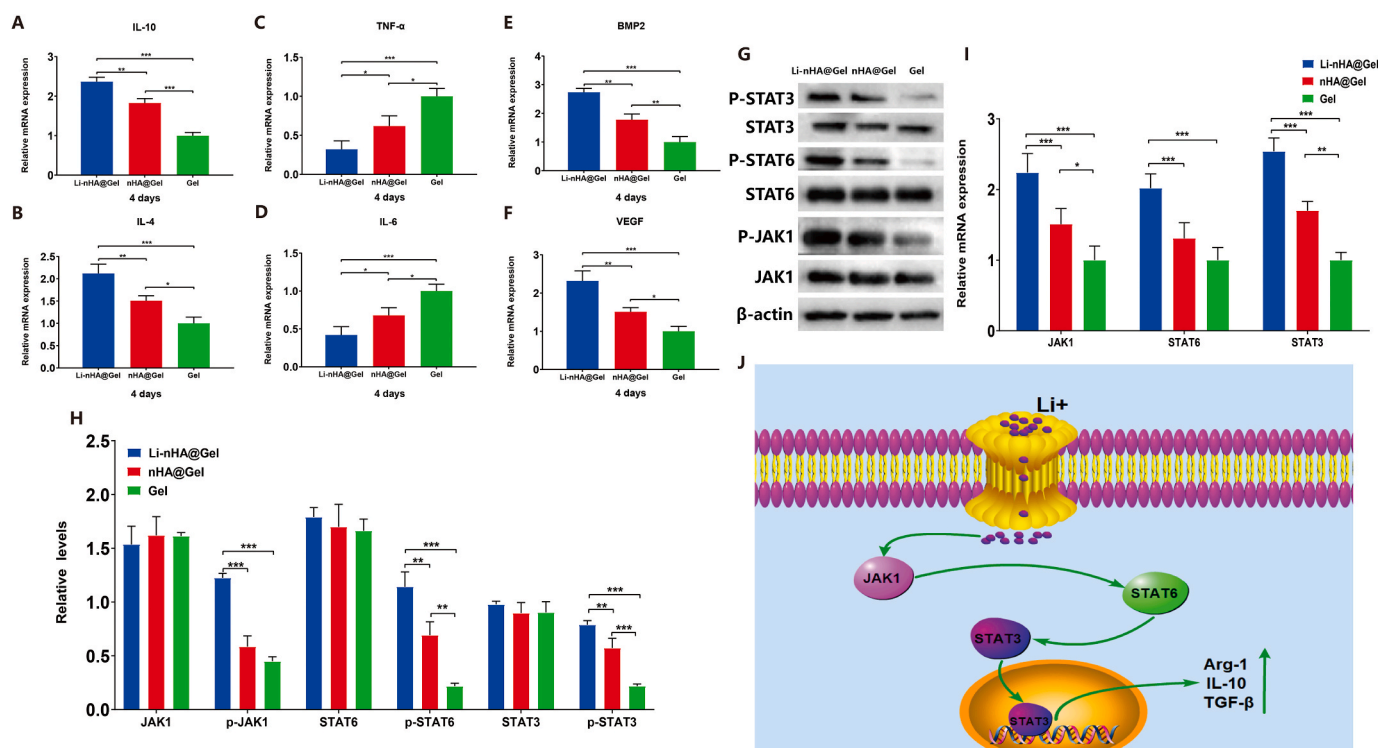


Fig. 5. Li-nHA@Gel regulates the inflammatory response of macrophages. (A–F) The phenotypic factors (TNF- α , IL-6, IL-10, IL-4), BMP2 and VEGF of M1 and M2 were quantitatively analyzed by RT-PCR. (G–I) The genes and proteins of JAK/STAT signaling pathway related factors (JAK1, STAT6, STAT3) were quantified by RT-PCR (I) and Western-blot (G–H). (J) Schematic summary of the molecular mechanism of Li⁺ mediating the polarization of M2 macrophages through JAK1/STAT6/STAT3 pathway and secreting osteogenic and angiogenic factors (BMP2 and VEGF). (*P < 0.05, **P < 0.01, and ***P < 0.001 represent statistically significant differences between groups).

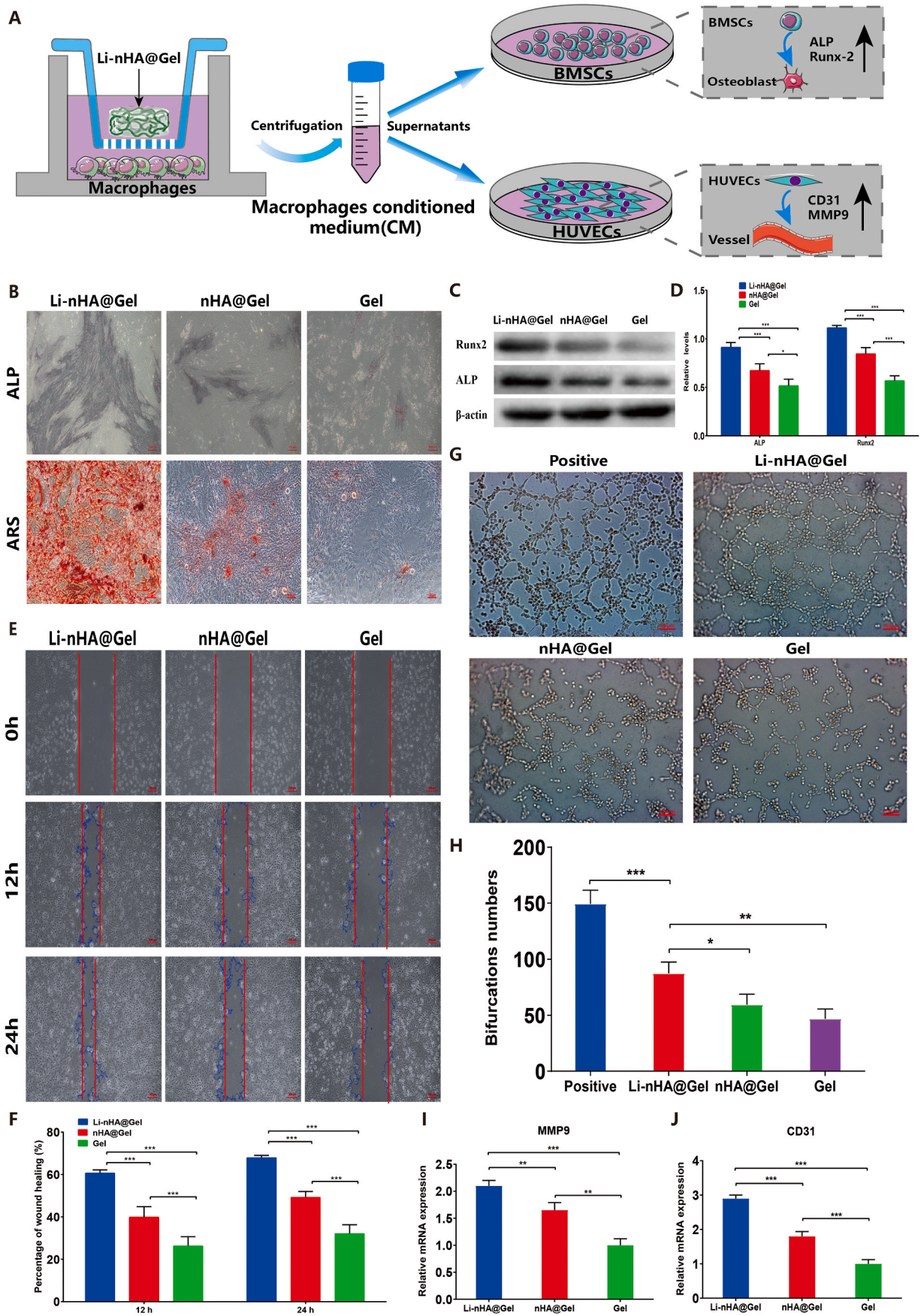
3.4. Li-nHA@Gel enhanced M2 macrophage polarization in vitro

To investigate the immunomodulatory properties of the hydrogel composites, macrophage polarization was assessed using flow cytometric analysis combined with immunofluorescence staining. RAW264.7 macrophages in the dormant state (M0) were first stimulated with dexamethasone to mimic the GCs induced osteonecrosis environment, and then their phenotype was assessed after incubation with hydrogel composites. M0 macrophages were round in shape, while dexamethasone-stimulated cells were shuttle-shaped (Fig. S7). The flow cytometric analysis results were shown in Fig. 4A–C and Fig. S8. The blank control has both low CCR7 and CD163 positive cells, whereas M1 induced group (LPS⁺) have significantly high CCR7 positive cells and M2 induced group (LPS⁺) have significantly high CD163 positive cells. For GCs group, the M1 phenotype was induced that evidenced by significantly high CCR7 positive cells, which demonstrated the mimicking of the osteonecrosis environment. When the cells were treated with the hydrogel composites, it was shown that the Li-nHA@Gel group had the highest percentage of M2 positive cells (F4/80 and CD163 double positive cells) as $36.1 \pm 5.5\%$, followed by the nHA@Gel group ($21.8 \pm 5.6\%$) and the Gel group ($9.56 \pm 2.6\%$), while the proportion of the M1-positive cells (F4/80 and CCR7 double positive cells) in the Li-nHA@Gel group ($30.3 \pm 4.4\%$) was lower than that of the nHA@Gel group ($44.7 \pm 4.9\%$) and the Gel group ($56 \pm 4\%$), indicating that the Li-nHA@Gel group enhanced the M2 macrophage polarization.

The immunofluorescence staining results were shown in Fig. 4D–F and Fig. S9. Similarly, the Li-nHA@Gel group shown a number of Arg-1 positive cells and a few of CCR7 negative cells, while the number of Arg-1 positive cells was decreased but the CCR7 negative cells was increased in nHA@Gel and Gel groups. When semi-quantitatively analyzed the integral optical density of fluorescence, Li-nHA@Gel significantly

improves the Arg-1 fluorescence than the other two groups ($p < 0.05$), while the CCR7 fluorescence intensity was lower than them ($p < 0.05$). Combined with the flow cytometric results, it indicates that the M2 is more activated in Li-nHA@Gel, while the other two groups have more M1 activation. Moreover, when compared to the nHA@Gel group, it was suggested that the Li⁺ release may be contribute to the enhanced M2 polarization.

The interaction of biomaterials with immune cells is crucial to achieve the desired bone repair outcome [55]. Among the many immune cells, macrophages play an important role in immune defense, and a specific macrophage phenotype is essential for tissue regeneration. Pro-inflammatory M1 macrophages produce inflammatory mediators such as CCR7, IL-1 β and TNF- α to mediate the inflammatory response, while anti-inflammatory M2 macrophages release pro-tissue repair factors such as Arg-1, IL-10, and TGF- β to maintain tissue homeostasis and promote tissue repair [56]. The typical immunomodulatory mechanism of biomaterials for tissue repair is the change of macrophage phenotype from pro-inflammatory M1 to anti-inflammatory M2 [57,58]. In the GI-ONFH lesion sites, there are a large number of M1 macrophages in the area of osteonecrosis and excess M1 macrophages cause bone resorption, which is an essential agent in the failure of osteonecrosis repair [3–5]. Therefore, for repair of osteonecrosis, it is necessary to induce a smooth and timely transition from high levels of M1 macrophages to pro-repair M2 macrophages in the osteonecrosis region. Accordingly, some studies have taken measures, e.g., intraperitoneal injection of IL-4, to facilitate the conversion of M1 cells to the M2 phenotype in areas of osteonecrosis and thus repair GI-ONFH [59,60]. In terms of bioactive ions, lithium plays an important role in balancing bone metabolism and bone formation and is capable of immunomodulation [29,31,32]. In the present study, we successfully doped a low dose of lithium into nHA and achieved a sustain and longterm release of Li⁺, and demonstrated that Li-nHA@Gel enhanced M2 macrophage



(caption on next page)

Fig. 6. Effect of macrophage polarization on BMSCs osteogenesis and HUVECs angiogenesis. (A) The illustration of experimental design. (B) BMSCs were treated with ARS staining and ALP staining under different conditioned medium. The scale is 100 μm . (C and D) Western blot was used to detect the expression of Runx2 and ALP in BMSCs 3 days after different conditioned medium treatments. (E and F) Scratch assay and wound healing rate of HUVECs treated by different conditioned medium for 12 and 24 h. The red line shows the linear scratches/wounds of each group of cells. The scale is 200 μm . (G and H) The tube formation assay and vascular branch number of HUVECs treated by different conditioned medium for 8 h. The scale is 100 μm . (I and J) Expression of vascular related factors CD31 (J) and MMP9 (I) in HUVECs after 3 days of different conditioned medium treatments. (* $P < 0.05$, ** $P < 0.01$, and *** $P < 0.001$ represent statistically significant differences between groups). (For interpretation of the references to color in this figure legend, the reader is referred to the Web version of this article.)

polarization.

3.5. Li-nHA@Gel activated JAK1/STAT6/STAT3 signaling pathway

As noted, the M1 and M2 phenotypes have identifiable markers on the cytokine secretion profile [61]. Therefore, we used real-time polymerase chain reaction (RT-PCR) to detect the relative expression levels of M1 and M2, osteogenesis and angiogenesis related gene markers. As shown in Fig. 5A–D, both the M2 gene markers IL-10 and IL-4 in Li-nHA@Gel group were significantly higher than that of nHA@Gel group ($p < 0.05$), while the expression trends of M1 gene markers TNF- α and IL-6 were opposite in the three groups, namely, Li-nHA@Gel < nHA@Gel < Gel group. In addition, the gene expression levels of osteoblastic and angiogenic cytokines (BMP-2 and VEGF) secreted by M2 macrophages were significantly upregulated in the Li-nHA@Gel group compared to nHA@Gel and Gel groups ($p < 0.05$) (Fig. 5E–F). These results suggested that Li-nHA@Gel not only enhanced the gene expression of M2 phenotypic polarization, but also upregulated the gene expression of osteoblastic and angiogenic cytokines.

Next, to further explore the potential mechanism of the enhancement of the M2 polarization, JAK1/STAT6/STAT3 pathway was chosen for investigating by Western Blot and RT-PCR analysis, since Li⁺ upregulates the expression level of IL-4. As shown in Fig. 5G–H, Li-nHA@Gel significantly increased the protein expression of phosphorylated JAK1, phosphorylated STAT6 and phosphorylated STAT3 compared with that in nHA@Gel and Gel groups, which may important for promoting the M2 cascade polarization in macrophages. Consistently, the results of quantitative RT-PCR analysis of the JAK1/STAT6/STAT3 signaling pathway shown similar trend (Fig. 5I). To summarize, we speculate that Li-nHA@Gel enhanced M2 macrophages polarization through the activation of the JAK1/STAT6/STAT3 signaling pathway (Fig. 5J).

3.6. Immunomodulation enhanced osteogenic and angiogenic differentiation in vitro

After implantation to the lesion sites, a large number of cells, including immune cells, bone marrow MSCs and endothelial cell, are recruited to the surrounding of the bone implant. Osteogenic differentiation of BMSCs in vivo is influenced not only by the properties of the implant surface but also by the surrounding immune microenvironment [62]. Therefore, the effect of immunomodulatory of the hydrogel composites on osteogenic and angiogenic differentiation in vitro using macrophage conditioned culture medium (CM) was investigated (Fig. 6A). The indirect effect of macrophages on osteogenic differentiation of BMSCs was assessed using Alizarin Red S (ARS) and ALP staining, and WB (ALP and Runx2). As shown in Fig. 6B–D, there are more ALP positive staining of BMSCs in the Li-nHA@Gel group than those in the other groups. And also, the calcium mineral deposition by ARS staining of BMSCs in the Li-nHA@Gel group was stronger than those in the other groups. Likewise, both Runx2 and ALP protein expression in Li-nHA@Gel was significantly higher than those in the other groups ($p < 0.05$). These results indicated that osteogenic differentiation of BMSCs were enhanced with the increasing levels of M2 polarization, and the synergistic effect of pro-M2 polarization and osteogenic differentiation was evident in the Li-nHA@Gel group.

The effect of macrophages conditioned culture medium on the angiogenesis of HUVECs was assessed using scratch assay, tube-forming assay, and RT-PCR. The scratch assay showed that with the extension of

the culture time, the scratch or wound area of each group decreased gradually. After culture for 12 and 24 h, the wound healing rate of the Gel group and the nHA@Gel group was lower than that of the Li-nHA@Gel group (Fig. 6E and F). Tube-forming assay showed that HUVECs cultured in Li-nHA@Gel and nHA@Gel conditioned medium enhanced angiogenesis after 8 h compared with that in Gel group (Fig. 6G). Moreover, Li-nHA@Gel group had significantly more vascular branches than those in the nHA@Gel and Gel group ($p < 0.05$) (Fig. 6H). RT-PCR results showed that the gene expression of CD31 and MMP9 in HUVECs cells was significantly higher in the Li-nHA@Gel group compared to nHA@Gel and Gel group ($p < 0.001$) (Fig. 6I and J). These results confirmed the ability of Li-nHA@Gel-derived CM to promote angiogenic differentiation of HUVECs in vitro.

Overall, it was found that the immune microenvironment induced by Li-nHA@Gel can promote the osteogenic differentiation of BMSCs as well as the angiogenic differentiation of HUVECs. Li-nHA@Gel can not only promote the expression of early osteogenic genes, but also promote calcium deposition, which may be related to the polarization of macrophages towards M2 under the action of Li⁺ and then the expression and secretion of BMP2, where BMP2 is a well-known growth factor that promotes osteogenic differentiation through the Smad1/5/9 signaling pathway [63], and thus Li-nHA@Gel stimulates the formation of an immune microenvironment that is conducive to enhance osteogenesis. Angiogenesis plays an important role in bone regeneration [64]. In the clinical progress of bone substitutes for osteonecrosis, a major challenge is to maintain the cell viability of the transplant center, which mainly depends on the rate of host vascular invasion [64,65]. Previous studies have tried to combine osteogenic and vascular growth factors for bone regeneration, however, the high cost limits its further clinical application [66]. In overview, the incorporation of immunoreactive Li⁺ facilitates the regulation of macrophage conversion from M1 to M2 phenotype, and the secreted cytokines provide an optimal microenvironment for bone immunomodulation, prompting immune enhancement of osteogenesis and angiogenesis, which will have potential to osteonecrosis treatment.

3.7. Li-nHA@Gel enhanced M2 macrophage polarization in vivo

The in vitro studies shown that the Li-nHA@Gel enhanced the M2 macrophage polarization, and promoted the osteogenesis and angiogenesis, which prompted us to further investigate its in vivo bone repair ability. A rabbit GI-ONFH model was constructed by using lipopolysaccharide and methylprednisolone induction before hydrogel composites were injected into the femoral head defect site, and the samples were taken out at the corresponding time points for relevant testing (Fig. 7A). The main procedure of the surgical procedure is shown in Fig. 7B.

Due to the immunomodulatory is crucial to achieve the desired bone repair outcome for GI-ONFH [59,60], the potential effect of hydrogel composites on macrophage polarization in vivo was first studied, though the enhanced M2 polarization have been evidenced in vitro studies. As shown in Fig. 7C—a large number of CCR7-positive cells and very rare Arg-1-positive cells were present in the osteonecrotic area in both Control and Gel groups, while nHA@Gel group had a greater number of Arg-1 cells and fewer CCR7 cells found in the osteonecrotic area. Likewise, Li-nHA@Gel group had plenty of Arg-1 cells and very poorly represented CCR7 cells in the osteonecrotic area. The fluorescence quantification analysis of Arg-1 showed that the Li-nHA@Gel group had

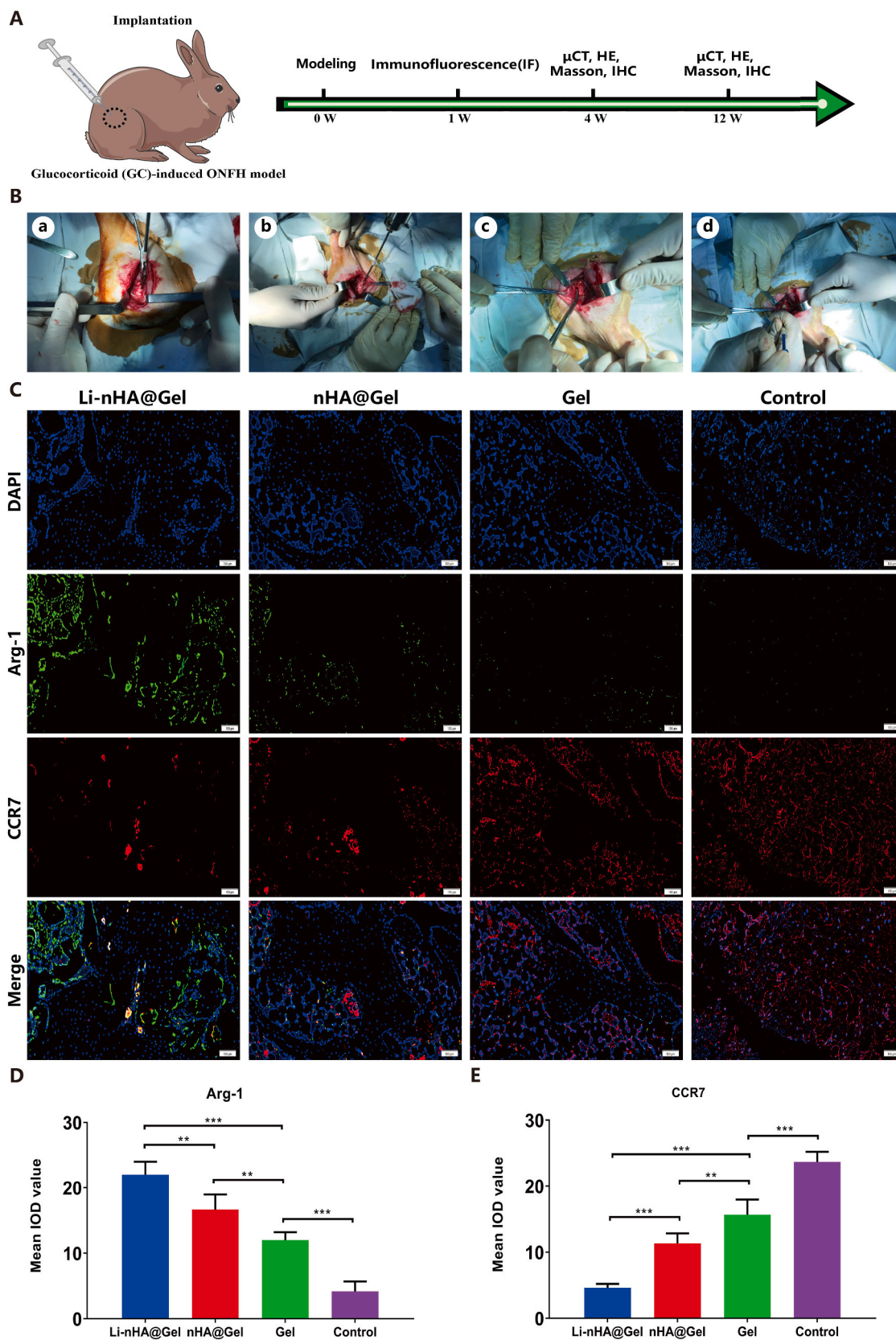


Fig. 7. Regulation of macrophage polarization in vivo by Li-nHA@Gel. (A). Schematic diagram of animal experimental steps. (B). Surgical procedure for hydrogel composites implantation into the femoral head: (a). Exposure to implantation area; (b). Drilling and core decompression; (c). A defect channel was made for bone grafting; (d). The hydrogel composites was implanted into the defect. (C). Macrophage phenotype in the defect area 1 week after hydrogel composites implantation: CCR7 (red, M1 macrophage marker); Arg-1 (green, M2 macrophage marker). The scale is 100 μ m. (D–E). Quantitative analysis of the IOD of Arg-1 and CCR7. (* $P < 0.05$, ** $P < 0.01$, and *** $P < 0.001$ represent statistically significant differences between groups). (For interpretation of the references to color in this figure legend, the reader is referred to the Web version of this article.)

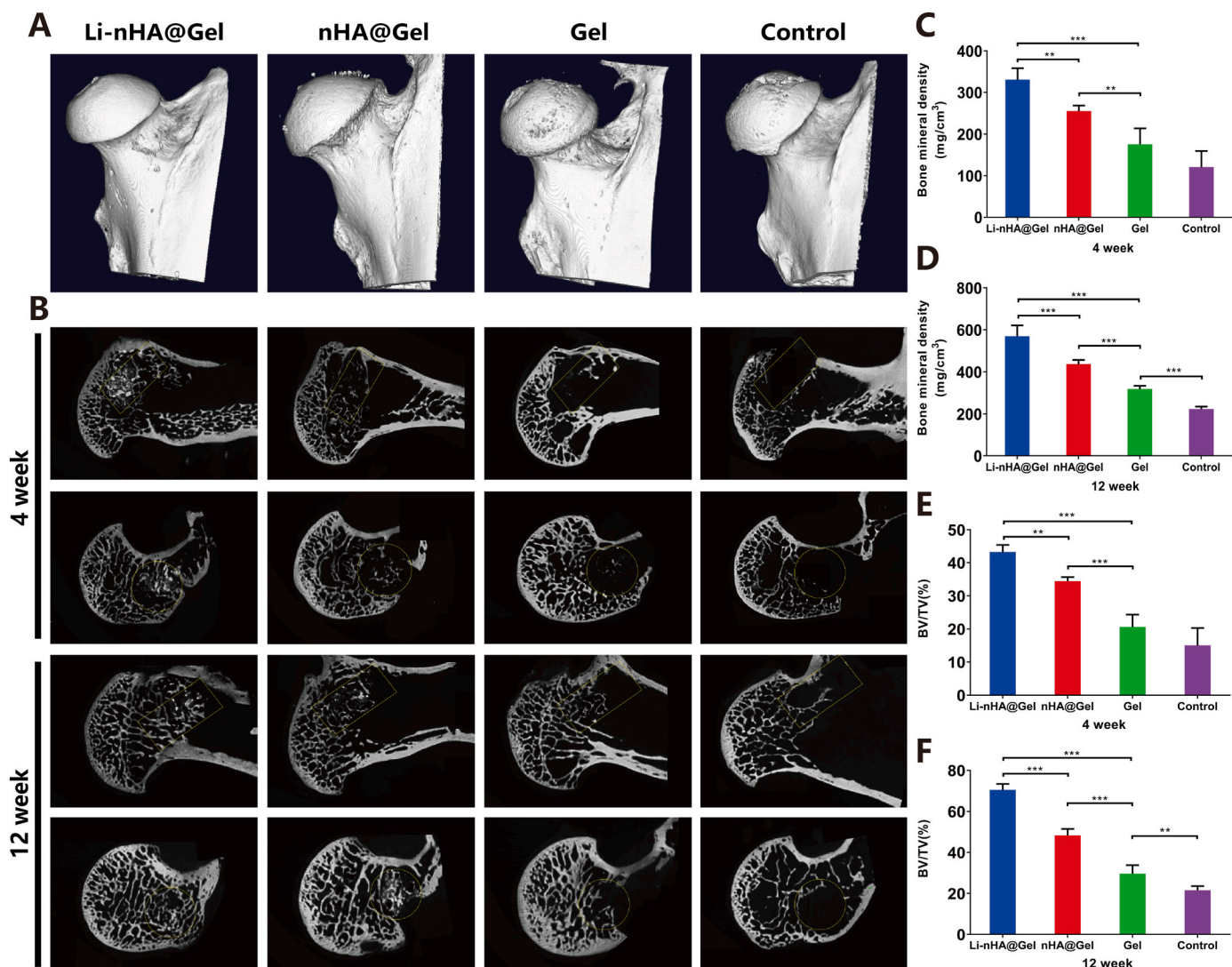


Fig. 8. New bone was formed in the drilling channel. (A) Micro-CT 3D reconstructed images. (B) Representative Micro-CT view of the femoral head in each group 4 and 12 weeks after implantation. Yellow circle and Yellow box shows the bone defect repair in the drilling channel. (C–F) Quantitative result of Micro-CT on BV/TV and bone mineral density of each group. (* $P < 0.05$, ** $P < 0.01$, and *** $P < 0.001$ represent statistically significant differences between groups). (For interpretation of the references to color in this figure legend, the reader is referred to the Web version of this article.)

the largest percentage of positive cells, followed by the nHA@Gel group, and both were larger than those in the Gel and Control groups (Fig. 7D). In contrast, the fluorescence quantification analysis of CCR7 showed the opposite trend, which means that the percentage of positive cells in the Li-nHA@Gel and nHA@Gel groups was lower than that in the other two groups (Fig. 7E). These results suggest that the addition of either Li-nHA or nHA nanoparticles to the hydrogel can alleviate the infiltration of M1 cells and promote the expression of M2 cells in the necrotic area, but the effect of Li-nHA nanoparticles was superior to that of nHA nanoparticles, suggesting that Li⁺ enhanced the M2 polarizing effect. Interestingly, we also found that the expression of Arg-1 cells in the Gel group was higher than that in the Control group, and the expression of CCR7 cells was lower than that in the Control group, which indicated that hydrogels have anti-inflammatory effects, which may relate with hyaluronic acid [67,68]. Previous studies have shown that excessive inflammatory responses leads to increased bone destruction resorption and inhibits osteogenic differentiation and bone regeneration, which subsequently leads to impaired osteonecrosis repair [69,70]. Here we revealed that Li-nHA@Gel effectively reverses the poor pro-inflammatory microenvironment in osteonecrotic areas and reprograms macrophages to a pro-regenerative M2 phenotype in vivo, which is consistent with the in

vitro results.

3.8. Li-nHA@Gel enhanced bone formation and regeneration in vivo

Due to the fact that we have confirmed that Li-nHA@Gel enhanced M2 macrophage polarization and promoted osteogenic differentiation in vitro, we next evaluate new bone formation and regeneration using microcomputed tomography (Micro-CT) at 4th and 12th week after injection implantation of the hydrogel composites. Gross specimen view of the femoral head in each group at 12 weeks after implantation of the composite hydrogel material (Fig. S10). As shown in Fig. 8A–B and Fig. S11, the new bone tissue in the Control group was less and the defect was clearly visible after 4 weeks. A small amount of bone tissue was generated in Gel group, but the defect area was still obvious. In contrast, new bone was increased in the nHA@Gel group, and a large number of new formed bone was observed in the Li-nHA@Gel group. When it came to 12th week, only a small amount of mineralized tissue was observed in the control group, and it was mostly confined to the edges of the defect area, with discontinuous, slender, and sparse new bone trabeculae. In the Gel group, the defect area was partially repaired with a small amount of mineralized tissue yet the defect was still well clarified. On the

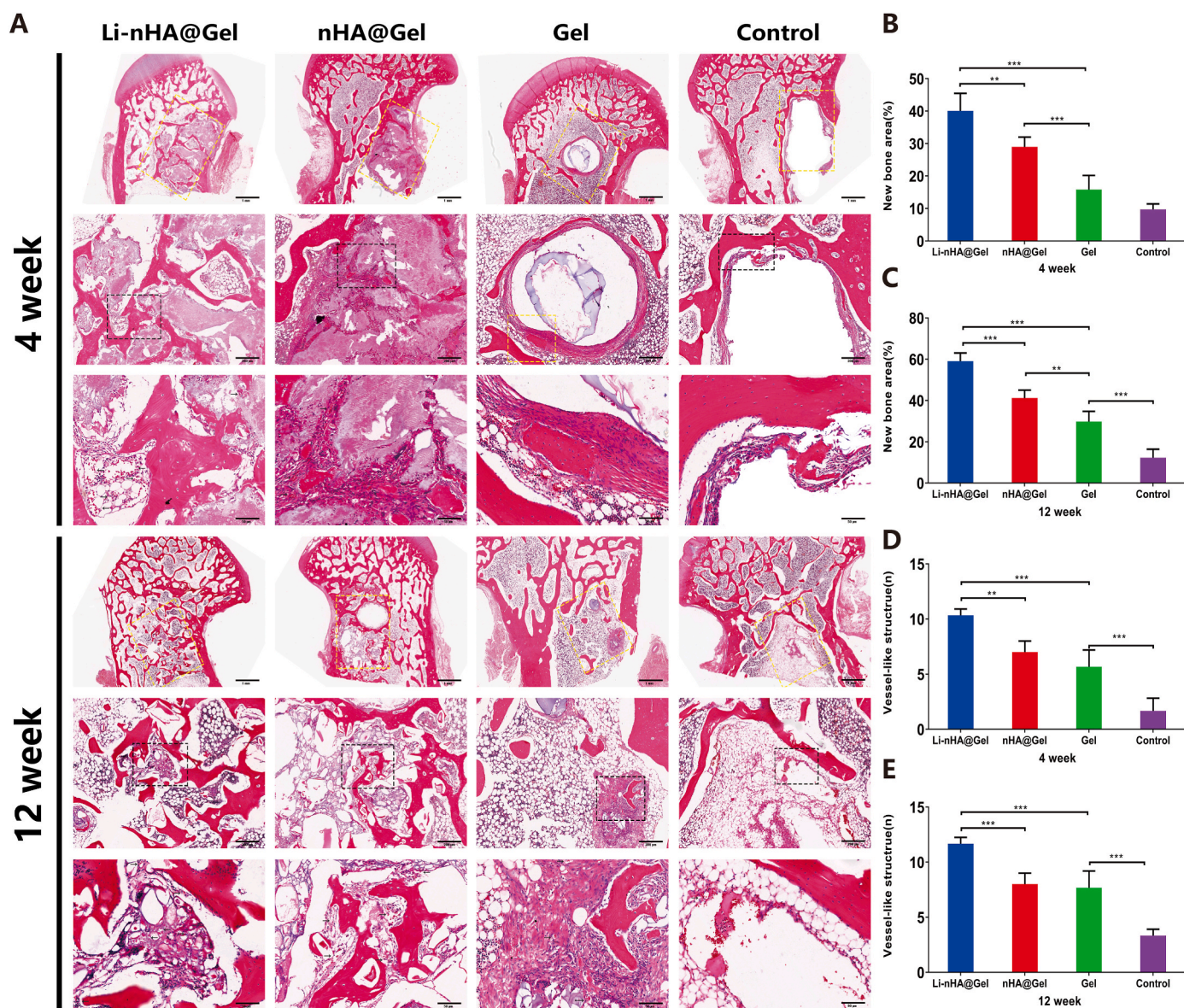


Fig. 9. Histological outcomes. (A) HE staining of bone defect specimens with femoral head osteonecrosis. Green arrows indicate the new formed blood vessels. Espbox shows the bone defect region and were magnified in on the image below. The scale is 1 mm, 200 μ m, 50 μ m. (B and C) Quantitative outcomes of the new bone formation. (D and E) Quantitative outcomes of new formed blood vessels number. (* $P < 0.05$, ** $P < 0.01$, and *** $P < 0.001$ represent statistically significant differences between groups). (For interpretation of the references to color in this figure legend, the reader is referred to the Web version of this article.)

contrary, the defect area was mostly repaired in the nHA@Gel group, and more mineralized tissue was present with a small area of unrepaired defect. Moreover, in the Li-nHA@Gel group, the bone defect area was almost completely repaired with the highest degree of mineralized bone tissue and tightly connected bone trabeculae.

Quantitative morphological analysis of bone regeneration using bone morphological parameters (BV/TV and bone mineral density (BMD)) was performed and the results showed that BMD and BV/TV were lower in the Gel and Control groups than those in the nHA@Gel and Li-nHA@Gel groups, with the highest BMD and BV/TV in the Li-nHA@Gel group (Fig. 8C–F), which revealed that nHA@Gel was capable of bone regeneration due to the contained nHA, while Li-nHA@Gel promoted bone regeneration more effectively compared with the nHA@Gel. In addition, Li-nHA@Gel increased the thickness and density of bone trabeculae, enhanced the coherence between new bone trabeculae, both of which may be more consistent with the mechanical properties required for osteonecrosis treatment. Taken together, these results suggest that Li-nHA@Gel has enhanced bone

formation and regeneration ability.

3.9. Histological analysis

To histologically investigate the repair ability of Li-nHA@Gel for osteonecrosis, H&E (Fig. 9A–E) and Masson's trichrome staining (Fig. 10) were used for analysis of new bone formation. At 4th week, the Control group only had a small amount of osteoid formation in the bone defect, and the Gel group had a larger osteoid area with a small number of vascular-like structure formation, while in the nHA@Gel group, the osteoid area in the bone defect was increased, so as the number of new vascular-like structures. The Li-nHA@Gel group had a large number of new formed bone and new blood vessels in the bone defects, with an area significantly larger than that of the other 3 groups. At week 12, it was found that most of the bone defects were still remained in the Control group, and a small amount of osteoid was seen in the periphery. In Gel group, a large amount of new osteoid tissue was found in the bone defect, but the formation of mature bone trabecula was rare. The bone

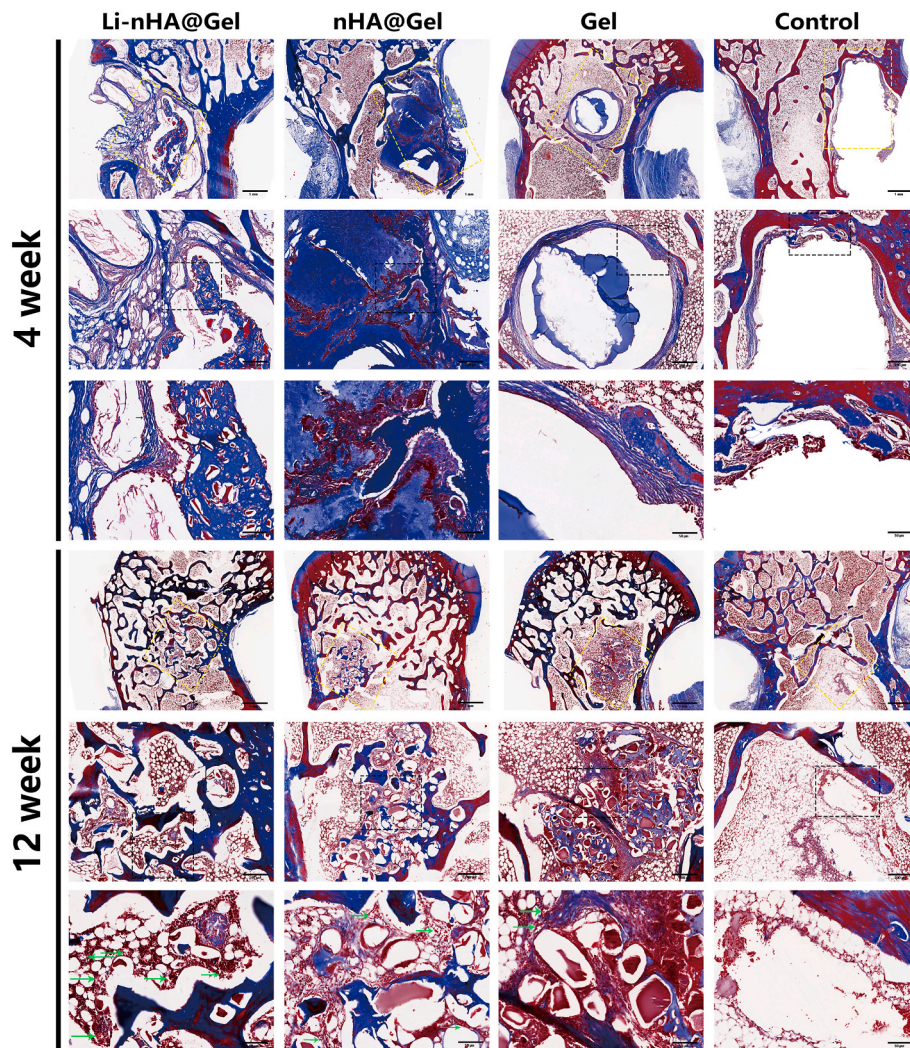


Fig. 10. Masson staining of specimens of bone defect. Green arrows indicate the new formed blood vessels. Espbox shows the bone defect region and were magnified in on the image below. The scale is 1 mm, 200 μ m, 50 μ m. (For interpretation of the references to color in this figure legend, the reader is referred to the Web version of this article.)

defect in nHA@Gel group was significantly reduced, and a large number of new osteoid tissues can be seen in the bone defect, and new blood vessels and bone trabecular formation were also observed. In the Li-nHA@Gel group, a large area of bone defect has been repaired, and mature bone trabecular arrangement can be seen in the bone defect, and a large number and area of new blood vessels are evident.

When quantitative analysis of the new bone formation, nHA@Gel achieved better new bone formation than the both Gel and control group ($p < 0.05$) at 4th week, but was inferior to the Li-nHA@Gel group ($p < 0.05$). When it came to the 12 week, it was found that the Li-nHA@Gel made best performance on new formed bone area ($p < 0.05$), while the nHA@Gel group took the second place and followed by Gel group and Control group ($p < 0.05$) (Fig. 9B and C). Meanwhile, we performed quantitative analysis of the number of the new blood vessels. The results revealed that the number of new blood vessels was higher in the Li-nHA@Gel group compared to other three groups ($p < 0.05$), and followed by the nHA@Gel and Gel group, which was superior to the Control group at both week 4 and week 12 ($p < 0.05$). These histopathological results are consistent with micro-CT analysis and confirmed that nHA@Gel is able to bone formation and repair, while Li-nHA@Gel promoted better bone repair and more new blood vessels formation.

3.10. Immunofluorescence analysis

Since in vitro studies have shown that Li-nHA@Gel promoted the osteogenic differentiation of BMSCs and the angiogenic differentiation of HUVECs, it is necessary to assess its in vivo osteogenic and angiogenic differentiation effects in osteonecrosis. Runx2 is a specific osteogenic differentiation transcription factor that regulates the gene transcription and contributes to the derivatization of MSCs to osteoblasts [39]. As shown in Fig. 11A and B, there was a large number of positive Runx2 cells in the Li-nHA@Gel group and has significantly higher mean IOD value compared to that of other groups ($p < 0.05$). The nHA@Gel group also had many positive Runx2 cells, followed by the Gel group, while Control group had little positive cells. Runx2 is an important marker of osteogenesis and is expressed at elevated levels in bone repair, especially in the late phase (12 weeks) [71]. Considering the role and impact of this protein in bone regeneration and repair, it may conclude that the Li-nHA@Gel has enhanced osteogenic capacity.

Platelet endothelial cell adhesion molecule-1 (CD31) is strongly expressed in vascular endothelium and vascular wall smooth muscle cells and can be used to evaluate vascular neogenesis [72,73]. As shown in Fig. 11C and D, Li-nHA@Gel group had the most and strongest CD31-positive staining vessels than that of the other three groups, while the nHA@Gel and Gel groups had similar but more CD31-positive vessel

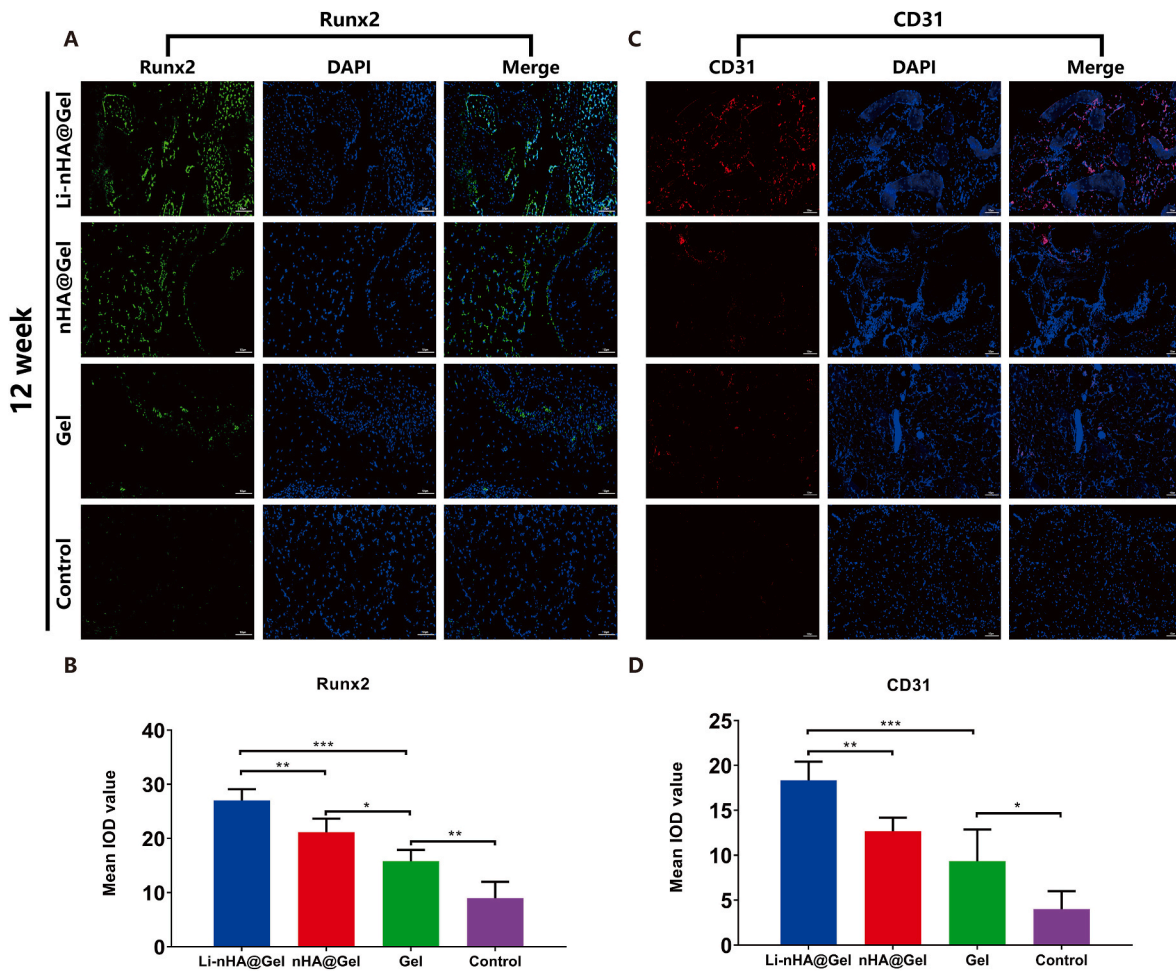


Fig. 11. Immunofluorescent staining for Runx2 and CD31 after scaffold implantation. (A)Immunofluorescent staining for Runx2 (green stained) and DAPI (blue) at 12 weeks after implantation. The scale is 100 μ m. (B)Quantitative analysis of the IOD of Runx2. (C) Immunofluorescent staining for CD31 (red stained) and DAPI (blue) at 12 weeks after implantation. The scale is 100 μ m. (D)Quantitative analysis of the IOD of CD31. (* $P < 0.05$, ** $P < 0.01$, and *** $P < 0.001$ represent statistically significant differences between groups). (For interpretation of the references to color in this figure legend, the reader is referred to the Web version of this article.)

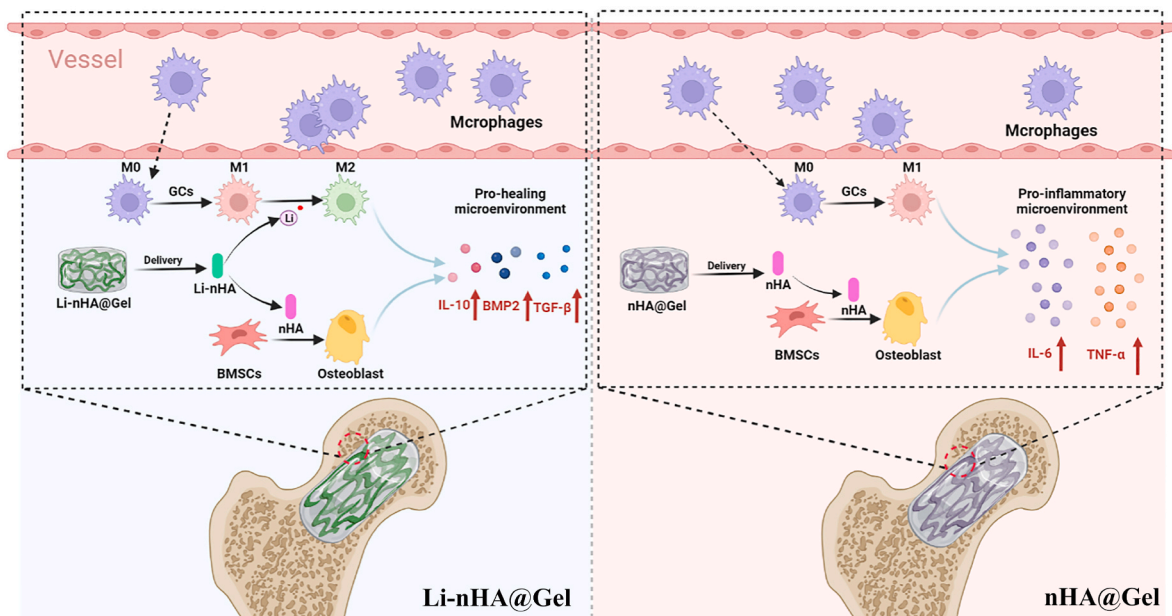


Fig. 12. Schematic diagram of the proposed mechanism of Li-nHA@Gel and nHA@Gel repair of osteonecrosis.

expression than that in Control group (Fig. 11C and D). Here, our in vivo outcomes were basically consistent with the in vitro results, indicating that Li-nHA@Gel has a strong ability to promote angiogenesis in vitro and in vivo, which will be beneficial to osteonecrosis.

3.11. Mechanism discussion

Immune regulation is recently a novel strategy for bone regeneration by combining osteoimmunity with immunomodulation [74]. Bone repairing materials with immunomodulatory properties activate the immune system and dynamically regulate the host bone immune microenvironment in situ to enhance bone regeneration and repair after implantation, wherein macrophages play a central role in coordinating the host immune response by releasing a series of cytokines and growth factors that affects the fate of the repairing [75]. In general, macrophages are activated through the classical activation pathway as M1 type, which is mainly pro-inflammatory and promotes the activation of the early inflammatory response, and through the alternative pathway as M2 type, which is mainly anti-inflammatory, promotes the resolution of the inflammatory response and facilitates osteogenesis and vascularization [76]. If there is an excess of M1 macrophages in the host bone immune microenvironment, this would lead to some local acute inflammatory responses or even a series of chronic inflammations that can block bone regeneration and repair [77], such as hormonal femoral head necrosis [41]. Therefore, modulating the polarization of macrophages towards the predominant M2 phenotype is beneficial in reducing local tissue inflammation and creating a favorable bone immune microenvironment.

Metal ions-mediated osteoimmunomodulation received considerable attention due to their high efficacy, however, the challenge lies in how to control their release in a relative low dose. Furthermore, the mechanism underlying the osteoimmunomodulation remains not completely clear. In the present study, we achieved a sustainable and longterm release profile of Li ions using a metal-doped and sulfhydryl groups binding method, and the evidence showed that Li-nHA@Gel enhanced the M2 macrophage polarization through the activation of the JAK1/STAT6/STAT3 signaling pathway. Here, based on the immune activity of Li-nHA@Gel to enhance the polarization of macrophages to M2, and the promotion effects of osteogenic and angiogenic differentiation both in vitro and in vivo, we proposed that the mechanism of Li-nHA@Gel repair of GI-ONFH as follows (Fig. 12). First, when the Li-nHA@Gel injected into the lesion site of GI-ONFH, the release of Li ions enhanced the switch from M1 macrophages to M2 cell phenotype in the osteonecrotic region, which decreased the pro-inflammatory reactions. Second, the enhanced M2 macrophage polarization upregulated the expression of the pro-tissue repair factors such as BMP2 and VEGF, thereby building a favorable osteoimmune microenvironment conducive to new bone and blood vessels formation. Meanwhile, nHA was capable of directly promoting the osteogenesis. Therefore, the above two synergistically build a microenvironment that promotes M2 macrophage polarization, osteogenesis and angiogenesis, and ultimately enhanced the bone regeneration and repair of osteonecrotic bone.

4. Conclusion

In summary, an injectable bone immunomodulatory biomaterial platform Li-nHA@Gel was constructed for the treatment of osteonecrosis in this work. The Li-nHA@Gel was capable of releasing Li⁺ in a sustainable and longterm manners, which enhanced the M2 macrophage polarization through the activation of the JAK1/STAT6/STAT3 signaling pathway, and then upregulated the pro-tissue repair factors VEGF and BMP-2 that promoted the osteogenic and angiogenic differentiation. In vivo study using a rabbit GI-ONFH model confirmed that Li-nHA@Gel enhanced M2 macrophage polarization, osteogenesis, and angiogenesis as well, which might contribute to the enhanced bone and blood vessel formation, and thus promoted bone regeneration. Overall,

this newly developed injectable bone immunomodulatory biomaterial platform with enhanced M2 macrophage polarization, osteogenesis, and angiogenesis will have a promising application in osteonecrosis treatment.

CRedit authorship contribution statement

Yue Luo: Methodology, Investigation, Writing – original draft, Conceptualization, Methodology, Investigation, Visualization. **Zhouyuan Yang:** Conceptualization, Methodology, Investigation, Visualization. **Xin Zhao:** Conceptualization, Methodology, Investigation, Visualization. **Donghai Li:** Investigation, Formal analysis. **Qianhao Li:** Methodology, Validation, Formal analysis. **Yang Wei:** Validation, Investigation, Formal analysis. **Luyao Wan:** Validation, Investigation, Formal analysis. **Meng Tian:** Methodology, Investigation, Writing – original draft, Conceptualization, Resources, Funding acquisition, Supervision, Writing – review & editing. **Pengde Kang:** Methodology, Investigation, Writing – original draft, Conceptualization, Resources, Funding acquisition, Supervision, Writing – review & editing.

Declaration of competing interest

The authors declare that they have no known competing financial interests or personal relationships that could have appeared to influence the work reported in this paper.

Data availability

No data was used for the research described in the article.

Acknowledgements

This study was supported by The National Natural Science Foundation of China (grant no. 81974333, 82172414 and 81401528), Project of Doctoral Research Initiation Fund, Sichuan North Medical College, China (Grant No. CBY23-QDA23), Science and Technology Program of Chengdu (grant no.2019-YF05-01188-SN), China Postdoctoral Science Foundation (Grant NO. 2021 M702338), the Fundamental Research Funds for the Central Universities (2022SCU12035) and Post-Doctor Research Project, West China Hospital, Sichuan University (2021HXBH049). The authors thank Li Li, and Fei Chen from the Institute of Clinical Pathology, West China Hospital of Sichuan University, for processing histological staining. The authors are grateful to Hongying Chen, Bo Su, Yue Li, Lei Wu, Jie Zhang, and Yan Wang of the Research Public Platform Service Platform of West China Hospital of Sichuan University for their assistance and guidance. The authors also thank Zheng Xiang from Laboratory of Electron Microscopy, West China School of Basic Medical Sciences, Sichuan University for biological transmission electron microscope preparation and observation.

Appendix A. Supplementary data

Supplementary data to this article can be found online at <https://doi.org/10.1016/j.mtbio.2024.100976>.

References

- [1] A. Cohen-Rosenblum, Q. Cui, Osteonecrosis of the femoral head, *Orthop Clin North Am* 50 (2) (2019) 139–149, <https://doi.org/10.1016/j.joc.2018.10.001>.
- [2] M.A. Mont, H.S. Salem, N.S. Piuizzi, S.B. Goodman, L.C. Jones, Nontraumatic osteonecrosis of the femoral head: where Do we stand today?: a 5-year update, *J Bone Joint Surg Am* 102 (12) (2020) 1084–1099, <https://doi.org/10.2106/JBJS.19.01271>.
- [3] C. Jiang, Z. Zhou, Y. Lin, H. Shan, W. Xia, F. Yin, N. Wang, L. Zhou, Y. Gao, X. Yu, Astragaloside IV ameliorates steroid-induced osteonecrosis of the femoral head by repolarizing the phenotype of pro-inflammatory macrophages, *Int. Immunopharm.* 93 (2021) 107345, <https://doi.org/10.1016/j.intimp.2020.107345>.

- [4] B. Fang, D. Wang, J. Zheng, Q. Wei, D. Zhan, Y. Liu, X. Yang, H. Wang, G. Li, W. He, L. Xu, Involvement of tumor necrosis factor alpha in steroid-associated osteonecrosis of the femoral head: friend or foe? *Stem Cell Res. Ther.* 10 (1) (2019) 5, <https://doi.org/10.1186/s13287-018-1112-x>.
- [5] N.S. Adapala, R. Yamaguchi, M. Phipps, O. Aruwajoye, H.K.W. Kim, Necrotic bone stimulates proinflammatory responses in macrophages through the activation of toll-like receptor 4, *Am. J. Pathol.* 186 (11) (2016) 2987–2999, <https://doi.org/10.1016/j.ajpath.2016.06.024>.
- [6] W. Cai, X. Xu, Y. Jiang, K. Cheng, F. Liu, C. Song, D. Guo, Z. Hu, Z. Liu, Z. Liu, Programmed release of hydrogel microspheres via regulating the immune microenvironment to promotes bone repair, *Mat. Today Advan.* 18 (2023) 100381, <https://doi.org/10.1016/j.mtadv.2023.100381>.
- [7] Y. Peng, J. Yang, W. Fu, Q. Gao, S. Yao, C. Peng, S. Hou, Osteoimmunomodulatory properties of a magnesium-doped phase-transited lysozyme coating on titanium, *Mat. Today Advan.* 14 (2022) 100234, <https://doi.org/10.1016/j.mtadv.2022.100234>.
- [8] Z. Xu, L. Wu, Y. Tang, K. Xi, J. Tang, Y. Xu, J. Xu, J. Lu, K. Guo, Y. Gu, L. Chen, Spatiotemporal regulation of the bone immune microenvironment via dam-like biphasic bionic periosteum for bone regeneration, *Adv. Healthcare Mater.* 12 (1) (2023) e2201661, <https://doi.org/10.1002/adhm.202201661>.
- [9] Q. Wei, Y. Su, H. Xin, L. Zhang, J. Ding, X. Chen, Immunologically effective biomaterials, *ACS Appl. Mater. Interfaces* 13 (48) (2021) 56719–56724, <https://doi.org/10.1021/acsmi.1c14781>.
- [10] J. Zhang, D. Tong, H. Song, R. Ruan, Y. Sun, Y. Lin, J. Wang, L. Hou, J. Dai, J. Ding, H. Yang, Osteoimmunity-regulating biomimetically hierarchical scaffold for augmented bone regeneration, *Adv. Mater.* 34 (36) (2022) e2202044, <https://doi.org/10.1002/adma.202202044>.
- [11] S. Qian, B. Zhao, J. Mao, Z. Liu, Q. Zhao, B. Lu, X. Mao, L. Zhang, L. Cheng, Y. Zhang, W. Cui, X. Sun, Biomedical applications of Janus membrane, *Biomedical Technology* 2 (2023) 58–69, <https://doi.org/10.1016/j.bmt.2022.11.003>.
- [12] Y. Peng, Z. Zhang, W. Tang, Y. Dai, Gel/hydrogel-based in situ biomaterial platforms for cancer postoperative treatment and recovery, *Explorations* 3 (5) (2023) 20220173, <https://doi.org/10.1002/EXP.20220173>.
- [13] Q. Wang, Y. Peng, M. He, W. Zhao, L. Qiu, C. Zhao, A hierarchical Janus nanofibrous membrane combining direct osteogenesis and osteoimmunomodulatory functions for advanced bone regeneration, *Adv. Funct. Mater.* 31 (8) (2021) 2008906, <https://doi.org/10.1002/adfm.202008906>.
- [14] X. Liu, W. Chen, B. Shao, X. Zhang, Y. Wang, S. Zhang, W. Wu, Mussel patterned with 4D biodegrading elastomer durably recruits regenerative macrophages to promote regeneration of craniofacial bone, *Biomaterials* 276 (2021) 120998, <https://doi.org/10.1016/j.biomaterials.2021.120998>.
- [15] C. Deng, Q. Zhou, M. Zhang, T. Li, H. Chen, C. Xu, Q. Peng, X. Wang, F. Yin, Y. Cheng, C. Wu, Bio ceramic scaffolds with antioxidative functions for ROS scavenging and osteochondral regeneration, *Adv. Sci.* 9 (12) (2022) e2105727, <https://doi.org/10.1002/advs.202105727>.
- [16] L.F. Velasquez-Garcia, Y. Kornbluth, Biomedical applications of metal 3D printing, *Annu. Rev. Biomed. Eng.* 23 (2021) 307–338, <https://doi.org/10.1146/annurev-bioeng-082020-032402>.
- [17] X. Sun, Z. Ma, X. Zhao, W. Jin, C. Zhang, J. Ma, L. Qiang, W. Wang, Q. Deng, H. Yang, J. Zhao, Q. Liang, X. Zhou, T. Li, J. Wang, Three-dimensional bioprinting of multicell-laden scaffolds containing bone morphogenic protein-4 for promoting M2 macrophage polarization and accelerating bone defect repair in diabetes mellitus, *Bioact. Mater.* 6 (3) (2021) 757–769, <https://doi.org/10.1016/j.bioactmat.2020.08.030>.
- [18] D. Barati, K. Watkins, Z. Wang, F. Yang, Injectable and crosslinkable PLGA-based microribbons as 3D macroporous stem cell niche, *Small* 16 (22) (2020) e1905820, <https://doi.org/10.1002/sml.201905820>.
- [19] R. Liu, S. Chen, P. Huang, G. Liu, P. Luo, Z. Li, Y. Xiao, Z. Chen, Z. Chen, Immunomodulation-based strategy for improving soft tissue and metal implant integration and its implications in the development of metal soft tissue materials, *Adv. Funct. Mater.* 30 (21) (2020) 1910672, <https://doi.org/10.1002/adfm.201910672>.
- [20] X. Xue, Y. Hu, Y. Deng, J. Su, Recent advances in design of functional biocompatible hydrogels for bone tissue engineering, *Adv. Funct. Mater.* 31 (19) (2021) 2009432, <https://doi.org/10.1002/adfm.202009432>.
- [21] P. Pal, M.A. Tucci, L.W. Fan, R. Bollavarapu, J.W. Lee, S.M. Salazar Marrocho, A. V. Janorkar, Functionalized collagen/elastin-like polypeptide hydrogels for craniofacial bone regeneration, *Adv. Healthcare Mater.* 12 (8) (2023) e2202477, <https://doi.org/10.1002/adhm.202202477>.
- [22] Z. Luo, Y. Wang, Y. Xu, J. Wang, Y. Yu, Modification and Crosslinking Strategies for Hyaluronic Acid-Based Hydrogel Biomaterials, *Smart Medicine* n/a, 2023 e20230029, <https://doi.org/10.1002/SMMD.20230029> n/a.
- [23] F. Lin, Y. Li, W. Cui, Injectable hydrogel microspheres in cartilage repair, *Biomedical Technology* 1 (2023) 18–29, <https://doi.org/10.1016/j.bmt.2022.11.002>.
- [24] D.K. Patel, S.D. Dutta, J. Hexiu, K. Ganguly, K.T. Lim, 3D-printable chitosan/silk fibroin/cellulose nanoparticle scaffolds for bone regeneration via M2 macrophage polarization, *Carbohydr. Polym.* 281 (2022) 119077, <https://doi.org/10.1016/j.carbpol.2021.119077>.
- [25] M.C.P. Sok, N. Baker, C. McClain, H.S. Lim, T. Turner, L. Hymel, M. Ogle, C. Olingy, J.I. Palacios, J.R. Garcia, K. Srithar, A.J. Garcia, P. Qiu, E.A. Botchwey, Dual delivery of IL-10 and AT-RvD1 from PEG hydrogels polarize immune cells towards pro-regenerative phenotypes, *Biomaterials* 268 (2021) 120475, <https://doi.org/10.1016/j.biomaterials.2020.120475>.
- [26] K. Zhang, Z. Jia, B. Yang, Q. Feng, X. Xu, W. Yuan, X. Li, X. Chen, L. Duan, D. Wang, L. Bian, Adaptable hydrogels mediate cofactor-assisted activation of biomarker-responsive drug delivery via positive feedback for enhanced tissue regeneration, *Adv. Sci.* 5 (12) (2018) 1800875, <https://doi.org/10.1002/advs.201800875>.
- [27] Z. Li, H. Wang, K. Zhang, B. Yang, X. Xie, Z. Yang, L. Kong, P. Shi, Y. Zhang, Y. P. Ho, Z.Y. Zhang, G. Li, L. Bian, Bisphosphonate-based hydrogel mediates biomimetic negative feedback regulation of osteoclastic activity to promote bone regeneration, *Bioact. Mater.* 13 (2022) 9–22, <https://doi.org/10.1016/j.bioactmat.2021.11.004>.
- [28] X. Chen, B. Tan, S. Wang, R. Tang, Z. Bao, G. Chen, S. Chen, W. Tang, Z. Wang, C. Long, W.W. Lu, D. Yang, L. Bian, S. Peng, Rationally designed protein cross-linked hydrogel for bone regeneration via synergistic release of magnesium and zinc ions, *Biomaterials* 274 (2021) 120895, <https://doi.org/10.1016/j.biomaterials.2021.120895>.
- [29] F. Peng, L. Qiu, M. Yao, L. Liu, Y. Zheng, S. Wu, Q. Ruan, X. Liu, Y. Zhang, M. Li, P. K. Chu, A lithium-doped surface inspires immunomodulatory functions for enhanced osteointegration through PI3K/AKT signaling axis regulation, *Biomater. Sci.* 9 (24) (2021) 8202–8220, <https://doi.org/10.1039/d1bm01075a>.
- [30] Q. Huang, Z. Ouyang, Y. Tan, H. Wu, Y. Liu, Activating macrophages for enhanced osteogenic and bactericidal performance by Cu ion release from micro/nanotopographical coating on a titanium substrate, *Acta Biomater.* 100 (2019) 415–426, <https://doi.org/10.1016/j.actbio.2019.09.030>.
- [31] C. Yang, W. Wang, K. Zhu, W. Liu, Y. Luo, X. Yuan, J. Wang, T. Cheng, X. Zhang, Lithium chloride with immunomodulatory function for regulating titanium nanoparticle-stimulated inflammatory response and accelerating osteogenesis through suppression of MAPK signaling pathway, *Int. J. Nanomed.* 14 (2019) 7475–7488, <https://doi.org/10.2147/IJN.S210834>.
- [32] M. Bartnikowski, H.J. Moon, S. Ivanovski, Release of lithium from 3D printed polycaprolactone scaffolds regulates macrophage and osteoclast response, *Biomed. Mater.* 13 (6) (2018) 065003, <https://doi.org/10.1088/1748-605X/aad916>.
- [33] J. Li, Q. Yao, Y. Xu, H. Zhang, L.L. Li, L. Wang, Lithium chloride-releasing 3D printed scaffold for enhanced cartilage regeneration, *Med. Sci. Mon. Int. Med. J. Exp. Clin. Res.* 25 (2019) 4041–4050, <https://doi.org/10.12659/MSM.916918>.
- [34] F. Shen, Y. Fang, Y. Wu, M. Zhou, J. Shen, X. Fan, Metal ions and nanometallic materials in antitumor immunity: function, application, and perspective, *J. Nanobiotechnol.* 21 (1) (2023) 20, <https://doi.org/10.1186/s12951-023-01771-z>.
- [35] R. Yang, G. Li, C. Zhuang, P. Yu, T. Ye, Y. Zhang, P. Shang, J. Huang, M. Cai, L. Wang, W. Cui, L. Deng, Gradient bimetallic ion-based hydrogels for tissue microstructure reconstruction of tendon-to-bone insertion, *Sci. Adv.* 7 (26) (2021), <https://doi.org/10.1126/sciadv.abg3816>.
- [36] S. Jiang, M. Wang, J. He, A review of biomimetic scaffolds for bone regeneration: toward a cell-free strategy, *Bioeng Transl Med* 6 (2) (2021) e10206, <https://doi.org/10.1002/btm2.10206>.
- [37] L. Kuang, X. Ma, Y. Ma, Y. Yao, M. Tariq, Y. Yuan, C. Liu, Self-assembled injectable nanocomposite hydrogels coordinated by in situ generated CaP nanoparticles for bone regeneration, *ACS Appl. Mater. Interfaces* 11 (19) (2019) 17234–17246, <https://doi.org/10.1021/acsmi.9b03173>.
- [38] Q. Zhang, L. Ma, X. Ji, Y. He, Y. Cui, X. Liu, C. Xuan, Z. Wang, W. Yang, M. Chai, X. Shi, High-strength hydroxyapatite scaffolds with minimal surface macrostructures for load-bearing bone regeneration, *Adv. Funct. Mater.* 32 (33) (2022) 2204182, <https://doi.org/10.1002/adfm.202204182>.
- [39] T. Zhu, M. Jiang, M. Zhang, L. Cui, X. Yang, X. Wang, G. Liu, J. Ding, X. Chen, Biofunctionalized composite scaffold to potentiate osteoconduction, angiogenesis, and favorable metabolic microenvironment for osteonecrosis therapy, *Bioact. Mater.* 9 (2022) 446–460, <https://doi.org/10.1016/j.bioactmat.2021.08.005>.
- [40] Y. Zhou, Z. Hu, W. Jin, H. Wu, M. Zuo, C. Shao, Y. Lan, Y. Shi, R. Tang, Z. Chen, Z. Xie, J. Shi, Intrafibrillar mineralization and immunomodulatory for synergistic enhancement of bone regeneration via calcium phosphate nanocluster scaffold, *Adv. Healthcare Mater.* 12 (12) (2023) e2201548, <https://doi.org/10.1002/adhm.202201548>.
- [41] M. Maruyama, S. Moeinzadeh, R.A. Guzman, N. Zhang, H.W. Storaci, T. Utsunomiya, E. Lui, E.E. Huang, C. Rhee, Q. Gao, Z. Yao, M. Takagi, Y.P. Yang, S. B. Goodman, The efficacy of lapine preconditioned or genetically modified IL4 over-expressing bone marrow-derived mesenchymal stromal cells in corticosteroid-associated osteonecrosis of the femoral head in rabbits, *Biomaterials* 275 (2021) 120972, <https://doi.org/10.1016/j.biomaterials.2021.120972>.
- [42] Y. Luo, D. Li, J. Zhao, Z. Yang, P. Kang, In vivo evaluation of porous lithium-doped hydroxyapatite scaffolds for the treatment of bone defect, *Bio Med. Mater. Eng.* 29 (6) (2018) 699–721, <https://doi.org/10.3233/BME-181018>.
- [43] D. Diaz-Jimenez, M.G. Petrillo, J.T. Busada, M.A. Hermoso, J.A. Cidowski, Glucocorticoids mobilize macrophages by transcriptionally up-regulating the exopeptidase DPP4, *J. Biol. Chem.* 295 (10) (2020) 3213–3227, <https://doi.org/10.1074/jbc.RA119.010894>.
- [44] Y. Luo, D. Li, X. Xie, P. Kang, Porous, lithium-doped calcium polyphosphate composite scaffolds containing vascular endothelial growth factor (VEGF)-loaded gelatin microspheres for treating glucocorticoid-induced osteonecrosis of the femoral head, *Biomed. Mater.* 14 (3) (2019) 035013, <https://doi.org/10.1088/1748-605X/ab0a55>.
- [45] Y. Wang, X. Yang, Z. Gu, H. Qin, L. Li, J. Liu, X. Yu, In vitro study on the degradation of lithium-doped hydroxyapatite for bone tissue engineering scaffold, *Mater. Sci. Eng., C* 66 (2016) 185–192, <https://doi.org/10.1016/j.msec.2016.04.065>.
- [46] P. Keikhosravani, H. Maleki-Ghaleh, A. Kahaie Khosrowshahi, M. Bodaghi, Z. Dargahi, M. Kavanlouei, P. Khademi-Azandehi, A. Fallah, Y. Beygi-Khosrowshahi, M.H. Siadati, Bioactivity and antibacterial behaviors of

- nanostructured lithium-doped hydroxyapatite for bone scaffold application, *Int. J. Mol. Sci.* 22 (17) (2021), <https://doi.org/10.3390/ijms22179214>.
- [47] V.P. Padmanabhan, S.N.T.S. N, S. Sagadevan, M.E. Hoque, R. Kulandaivelu, Advanced lithium substituted hydroxyapatite nanoparticles for antimicrobial and hemolytic studies, *New J. Chem.* 43 (47) (2019) 18484–18494, <https://doi.org/10.1039/C9NJ03735G>.
- [48] J. Xie, M. Bao, S.M.C. Bruekers, W.T.S. Huck, Collagen gels with different fibrillar microarchitectures elicit different cellular responses, *ACS Appl. Mater. Interfaces* 9 (23) (2017) 19630–19637, <https://doi.org/10.1021/acsami.7b03883>.
- [49] M. Liu, Y. Ishida, Y. Ebina, T. Sasaki, T. Hikima, M. Takata, T. Aida, An anisotropic hydrogel with electrostatic repulsion between cofacially aligned nanosheets, *Nature* 517 (7532) (2015) 68–72, <https://doi.org/10.1038/nature14060>.
- [50] J.A. Burdick, G.D. Prestwich, Hyaluronic acid hydrogels for biomedical applications, *Adv. Mater.* 23 (12) (2011) H41–H56, <https://doi.org/10.1002/adma.201003963>.
- [51] J. Yan, Y. Miao, H. Tan, T. Zhou, Z. Ling, Y. Chen, X. Xing, X. Hu, Injectable alginate/hydroxyapatite gel scaffold combined with gelatin microspheres for drug delivery and bone tissue engineering, *Mater. Sci. Eng., C* 63 (2016) 274–284, <https://doi.org/10.1016/j.msec.2016.02.071>.
- [52] Y. Huang, X. Zhang, A. Wu, H. Xu, An injectable nano-hydroxyapatite (n-HA)/glycol chitosan (G-CS)/hyaluronic acid (HyA) composite hydrogel for bone tissue engineering, *RSC Adv.* 6 (40) (2016) 33529–33536, <https://doi.org/10.1039/C5RA26160K>.
- [53] Y. Peng, Q.J. Liu, T. He, K. Ye, X. Yao, J. Ding, Degradation rate affords a dynamic cue to regulate stem cells beyond varied matrix stiffness, *Biomaterials* 178 (2018) 467–480, <https://doi.org/10.1016/j.biomaterials.2018.04.021>.
- [54] A.H. Lourenco, A.L. Torres, D.P. Vasconcelos, C. Ribeiro-Machado, J.N. Barbosa, M.A. Barbosa, C.C. Barrias, C.C. Ribeiro, Osteogenic, anti-osteoclastogenic and immunomodulatory properties of a strontium-releasing hybrid scaffold for bone repair, *Mater. Sci. Eng., C* 99 (2019) 1289–1303, <https://doi.org/10.1016/j.msec.2019.02.053>.
- [55] T. Ding, W. Kang, J. Li, L. Yu, S. Ge, An in situ tissue engineering scaffold with growth factors combining angiogenesis and osteoimmunomodulatory functions for advanced periodontal bone regeneration, *J. Nanobiotechnol.* 19 (1) (2021) 247, <https://doi.org/10.1186/s12951-021-00992-4>.
- [56] J.M. Olefsky, C.K. Glass, Macrophages, inflammation, and insulin resistance, *Annu. Rev. Physiol.* 72 (2010) 219–246, <https://doi.org/10.1146/annurev-physiol-021909-135846>.
- [57] J. Li, X. Jiang, H. Li, M. Gelinsky, Z. Gu, Tailoring materials for modulation of macrophage fate, *Adv. Mater.* 33 (12) (2021) e2004172, <https://doi.org/10.1002/adma.202004172>.
- [58] T. Wang, J. Bai, M. Lu, C. Huang, D. Geng, G. Chen, L. Wang, J. Qi, W. Cui, L. Deng, Engineering immunomodulatory and osteoinductive implant surfaces via mussel adhesion-mediated ion coordination and molecular clicking, *Nat. Commun.* 13 (1) (2022) 160, <https://doi.org/10.1038/s41467-021-27816-1>.
- [59] S.M. McCormick, N.M. Heller, Regulation of macrophage, dendritic cell, and microglial phenotype and function by the SOCS proteins, *Front. Immunol.* 6 (2015) 549, <https://doi.org/10.3389/fimmu.2015.00549>.
- [60] S. Jin, C. Meng, Y. He, X. Wang, Q. Zhang, Z. Wang, W. Huang, H. Wang, Curcumin prevents osteocyte apoptosis by inhibiting M1-type macrophage polarization in mice model of glucocorticoid-associated osteonecrosis of the femoral head, *J. Orthop. Res.* 38 (9) (2020) 2020–2030, <https://doi.org/10.1002/jor.24619>.
- [61] C. Li, C. Guo, V. Fitzpatrick, A. Ibrahim, M.J. Zwierstra, P. Hanna, A. Lechtig, A. Nazarian, S.J. Lin, D.L. Kaplan, Design of biodegradable, implantable devices towards clinical translation, *Nat. Rev. Mater.* 5 (1) (2020) 61–81, <https://doi.org/10.1038/s41578-019-0150-z>.
- [62] D.-W. Zhao, C. Liu, K.-Q. Zuo, P. Su, L.-B. Li, G.-Y. Xiao, L. Cheng, Strontium-zinc phosphate chemical conversion coating improves the osseointegration of titanium implants by regulating macrophage polarization, *Chem. Eng. J.* 408 (2021) 127362, <https://doi.org/10.1016/j.cej.2020.127362>.
- [63] C.L. Wang, F. Xiao, C.D. Wang, J.F. Zhu, C. Shen, B. Zuo, H. Wang, D. Li, X. Y. Wang, W.J. Feng, Z.K. Li, G.L. Hu, X. Zhang, X.D. Chen, Gremlin2 suppression increases the BMP-2-induced osteogenesis of human bone marrow-derived mesenchymal stem cells via the BMP-2/smad/runx2 signaling pathway, *J. Cell. Biochem.* 118 (2) (2017) 286–297, <https://doi.org/10.1002/jcb.25635>.
- [64] A. Grosso, M.G. Burger, A. Lungler, D.J. Schaefer, A. Banfi, N. Di Maggio, It takes two to tango: coupling of angiogenesis and osteogenesis for bone regeneration, *Front. Bioeng. Biotechnol.* 5 (2017) 68, <https://doi.org/10.3389/fbioe.2017.00068>.
- [65] H. Dong, T. Zhu, M. Zhang, D. Wang, X. Wang, G. Huang, S. Wang, M. Zhang, Polymer scaffolds-enhanced bone regeneration in osteonecrosis therapy, *Front. Bioeng. Biotechnol.* 9 (2021) 761302, <https://doi.org/10.3389/fbioe.2021.761302>.
- [66] Y.W. Su, R. Chung, C.S. Ruan, S.M. Chim, V. Kuek, P.P. Dwivedi, M. Hassanshahi, K.M. Chen, Y. Xie, L. Chen, B.K. Foster, V. Rosen, X.F. Zhou, J. Xu, C.J. Xian, Neurotrophin-3 induces BMP-2 and VEGF activities and promotes the bony repair of injured growth plate cartilage and bone in rats, *J. Bone Miner. Res.* 31 (6) (2016) 1258–1274, <https://doi.org/10.1002/jbmr.2786>.
- [67] L. Yu, P. Hu, Y. Chen, Gas-generating nanoplatforms: material chemistry, multifunctionality, and gas therapy, *Adv. Mater.* 30 (49) (2018) e1801964, <https://doi.org/10.1002/adma.201801964>.
- [68] A. Boddupalli, L. Zhu, K.M. Bratlie, Methods for implant acceptance and wound healing: material selection and implant location modulate macrophage and fibroblast phenotypes, *Adv. Healthcare Mater.* 5 (20) (2016) 2575–2594, <https://doi.org/10.1002/adhm.201600532>.
- [69] R.J. Miron, D.D. Bosshardt, OsteoMacs: key players around bone biomaterials, *Biomaterials* 82 (2016) 1–19, <https://doi.org/10.1016/j.biomaterials.2015.12.017>.
- [70] W. Liu, J. Li, M. Cheng, Q. Wang, K.W.K. Yeung, P.K. Chu, X. Zhang, Zinc-Modified sulfonated polyetheretherketone surface with immunomodulatory function for guiding cell fate and bone regeneration, *Adv. Sci.* 5 (10) (2018) 1800749, <https://doi.org/10.1002/adv.201800749>.
- [71] X. Liu, M.N. George, S. Park, A.L. Miller II, B. Gaihre, L. Li, B.E. Waletzki, A. Terzic, M.J. Yaszemski, L. Lu, 3D-printed scaffolds with carbon nanotubes for bone tissue engineering: fast and homogeneous one-step functionalization, *Acta Biomater.* 111 (2020) 129–140, <https://doi.org/10.1016/j.actbio.2020.04.047>.
- [72] R. Zhao, S. Chen, W. Zhao, L. Yang, B. Yuan, V.S. Ioan, A.V. Iulian, X. Yang, X. Zhu, X. Zhang, A bioceramic scaffold composed of strontium-doped three-dimensional hydroxyapatite whiskers for enhanced bone regeneration in osteoporotic defects, *Theranostics* 10 (4) (2020) 1572–1589, <https://doi.org/10.7150/thno.40103>.
- [73] P. Gao, B. Fan, X. Yu, W. Liu, J. Wu, L. Shi, D. Yang, L. Tan, P. Wan, Y. Hao, S. Li, W. Hou, K. Yang, X. Li, Z. Guo, Biofunctional magnesium coated Ti6Al4V scaffold enhances osteogenesis and angiogenesis in vitro and in vivo for orthopedic application, *Bioact. Mater.* 5 (3) (2020) 680–693, <https://doi.org/10.1016/j.bioactmat.2020.04.019>.
- [74] Z. Chen, T. Klein, R.Z. Murray, R. Crawford, J. Chang, C. Wu, Y. Xiao, Osteoimmunomodulation for the development of advanced bone biomaterials, *Mater. Today* 19 (6) (2016) 304–321, <https://doi.org/10.1016/j.mattod.2015.11.004>.
- [75] Y. Zhu, H. Liang, X. Liu, J. Wu, C. Yang, T.M. Wong, K.Y.H. Kwan, K.M.C. Cheung, S. Wu, K.W.K. Yeung, Regulation of macrophage polarization through surface topography design to facilitate implant-to-bone osteointegration, *Sci. Adv.* 7 (14) (2021), <https://doi.org/10.1126/sciadv.abf6654>.
- [76] C. Schlundt, T. El Khassawna, A. Serra, A. Dienelt, S. Wendler, H. Schell, N. van Rooijen, A. Radbruch, R. Lucius, S. Hartmann, G.N. Duda, K. Schmidt-Bleek, Macrophages in bone fracture healing: their essential role in endochondral ossification, *Bone* 106 (2018) 78–89, <https://doi.org/10.1016/j.bone.2015.10.019>.
- [77] Z. Lin, D. Shen, W. Zhou, Y. Zheng, T. Kong, X. Liu, S. Wu, P.K. Chu, Y. Zhao, J. Wu, K.M.C. Cheung, K.W.K. Yeung, Regulation of extracellular bioactive cations in bone tissue microenvironment induces favorable osteoimmune conditions to accelerate in situ bone regeneration, *Bioact. Mater.* 6 (8) (2021) 2315–2330, <https://doi.org/10.1016/j.bioactmat.2021.01.018>.